Elucidating the Impact of Mg Substitution on the Properties of NASICON-$Na_{3+y}V_{2-y}Mg_y(PO_4)_3$ Cathodes

Subham Ghosh,[‖,a,b,c,] Nabadyuti Barman,[‖,a,b,c] Eliovardo Gonzalez-Correa,[d,e] Madhulika Mazumder,[a,c,f] Aryan Zaveri,[e,g] Raynald Giovine,[d,e] Alexis Manche,[d,h,#] Swapan K. Pati,[c,f] Raphaële J. Clément,[d,e,] and Premkumar Senguttuvan [a,b,c,*]*

[a]New Chemistry Unit, [b]International Centre for Materials Science and [c]School of Advanced Materials, Jawaharlal Nehru Centre for Advanced Scientific Research, Jakkur, Bangalore-560064, India.

[d]Materials Department, University of California Santa Barbara, Santa Barbara, CA 93106-5050, USA.

[e]Materials Research Laboratory, University of California Santa Barbara, Santa Barbara, CA 93106-9530, USA.

[f]Theoretical Science Unit, Jawaharlal Nehru Centre for Advanced Scientific Research, Jakkur, Bangalore-560064, India.

[g]Physics Department, University of California Santa Barbara, Santa Barbara, CA 93106-9530, USA.

[h]Université de Bordeaux, UF Chimie, F-33405, Talence, France.

[#]Present address: School of Chemistry, University of St Andrews, North Haugh, St Andrews, KY16 9ST, United Kingdom.

Vanadium multi-redox based NASICON-$Na_zV_{2-y}M_y(PO_4)_3$ ($3 \leq z \leq 4$; M = Al^{3+}, Cr^{3+} and Mn^{2+}) cathodes are particularly attractive for Na-ion battery applications due to their high Na insertion voltage (>3.5 V vs. Na^+/Na^0), reversible storage capacity (~150 mA h g^{-1}) and rate performance. However, their practical application is hindered by rapid capacity fade due to bulk structural rearrangements at high potentials involving complex redox and local structural changes. To decouple these factors, we have studied a series of Mg^{2+} substituted $Na_{3+y}V_{2-y}Mg_y(PO_4)_3$ ($0 \leq y \leq 1$) cathodes for which the only redox-active species is vanadium. Whilst X-ray diffraction (XRD) confirms the formation of solid solutions between the y = 0 and 1 end members, X-ray absorption spectroscopy and solid-state nuclear magnetic resonance reveal a complex evolution of the local structure upon progressive Mg^{2+} substitution for V^{3+}. Concurrently, the intercalation voltage rises from 3.35 to 3.45 V, due to

increasingly more ionic V-O bonds, and the sodium (de)intercalation mechanism transitions from a two-phase for $y \leq 0.5$ to a solid solution process for $y \geq 0.5$, as confirmed by *in-operando* XRD, whilst Na-ion diffusion kinetics follow a non-linear trend across the compositional series.

1. INTRODUCTION

The successful utilization of renewable energy derived from intermittent sources, such as wind and solar, necessitates the employment of large-scale electrochemical energy storage devices.[1] Given their successful implementation in portable electronics and electric vehicle applications, Li-ion batteries are serious contenders for grid-level storage. However, the soaring price of lithium precursors and geopolitical uncertainty associated with their supply chain have encouraged researchers to develop alternative technologies. Among those, Na-ion batteries are very promising due to their inexpensive and Earth abundant precursors.[2] Over the past decade, a large number of Na-ion electrode and electrolyte materials have been discovered, in part thanks to the materials design knowledge gained from earlier investigations of Li-based systems and the similar properties of Li and Na alkali metals. However, the exploration of suitable Na-ion cathodes with high energy density, good rate performance and long cycle life remains critical. To this end, NA SuperIonic CONductor (NASICON)-type phosphate cathodes are particularly appealing because of their high insertion voltages and good sodium diffusivity, as well as excellent structural and thermal stabilities.[3]

The general chemical composition of transition metal-based NASICON phosphates can be written as $Na_zM_2(PO_4)_3$ ($0 \leq z \leq 4$; M = first and second row early transition metals).[4] Their three-dimensional crystal structure is generally described using a rhombohedral $R\bar{3}c$

space group and is built from so-called 'lantern' units, which consist of two MO_6 octahedra and three XO_4 tetrahedra, stacked along the *c*-direction. In this structure, Na^+ ions occupy two different crystallographic sites, namely 6*b* Na(1) and 18*e* Na(2), with a maximum number of four Na per formula unit. Earlier studies on $Na_3M_2(PO_4)_3$ (M = Ti, V, Cr and Fe) [5-8] have reported a maximum reversible exchange of two moles of Na per formula unit (*pfu*), corresponding to a one-electron redox process per transition metal center, leading to moderate charge storage capacities of ~100-120 mA h g^{-1}. One obvious avenue to improve the capacity of NASICON phosphate cathodes is to introduce multi-electron redox centers to enable the exchange of a larger number of sodium ions in the framework. From this viewpoint, the $Na_3V_2(PO_4)_3$ (NVP) cathode has received a lot of attention as V^{3+} can, in theory, undergo a two-electron redox process to form V^{5+} on charge, yet only $V^{4+/3+}$ redox has been realized experimentally.[9] This limitation has motivated several studies of *iso*- and *alio*-valent cationic substitutions into NVP to realize multi-electron $V^{5+}/V^{4+}/V^{3+}$ redox reactions.[10-16] This strategy has proven successful for *iso*-valently substituted cathodes, such as $Na_3V_{1.5}Al_{0.5}(PO_4)_3$ and $Na_3VCr(PO_4)_3$, which exhibit two step voltage profiles at 3.4 and 4.0 V corresponding to the redox activity of the V^{4+}/V^{3+} and V^{5+}/V^{4+} couples, respectively. Although the high intercalation voltage of the V^{5+}/V^{4+} couple leads to improvements in energy density compared to unsubstituted NVP, their intercalation capacities are similar to that of NVP (i.e., two moles of Na-ions exchanged *pfu*). Alternatively, aliovalent Mn^{2+} substitution into the NVP framework results in the formation of a fully sodiated NASICON-$Na_4VMn(PO_4)_3$ cathode.[17] When cycled between 3.75 and 2.5 V vs. Na^+/Na^0, this material exhibits two voltage plateaus at 3.4 (V^{4+}/V^{3+}) and 3.6 V (Mn^{3+}/Mn^{2+}) vs. Na^+/Na^0, but is again limited to two moles of reversible Na-ion exchange *pfu*. Upon extending the charge voltage window to 4.2 V vs. Na^+/Na^0, an additional one mole of sodium ions can be removed, raising the total

charge capacity of the $Na_4VMn(PO_4)_3$ cathode to 150 mA h g^{-1}.[18] This additional capacity has been attributed to the redox activities of the V^{5+}/V^{4+} and Mn^{4+}/Mn^{3+} couples. Unfortunately, on subsequent discharge, only 1.5 moles of Na^+ ions are reinserted into the structure. *In-operando* XRD studies have attributed this capacity loss to an irreversible structural transformation of the NASICON framework at high voltage, triggered by the removal of Na^+ ions from Na(1) sites and possible vanadium cation migration into them.[19,20] Further, the $Na_4VMn(PO_4)_3$ cathode displays rapid capacity fade upon cycling. Structural and capacity degradation upon high voltage cycling has also been observed in Mn-rich $Na_{3+y}V_{2-y}Mn_y(PO_4)_3$ cathodes.[21,22] However, it is not yet clear what role concomitant local structural and electronic processes occurring at higher voltages play in the abovementioned issues. Specifically, the interplay between the removal of Na^+ ions from Na(1) and Na(2) sites and the oxidation of V^{4+} to V^{5+} as well as Mn^{3+} to Mn^{4+} and associated changes to $(V/Mn)O_6$ local environments makes it difficult to separate individual contributions to the observed electrode degradation phenomena. Therefore, it is necessary to decouple structural and electronic processes to better understand the links between structure/composition and electrochemical properties.

In the present work, we have designed a series of Mg^{2+}-substituted NASICON cathodes with compositions $Na_{3+y}V_{2-y}Mg_y(PO_4)_3$ akin to previously-studied Mn^{2+}-substituted NVP compounds.[21,22] The electrochemical inactivity of Mg^{2+} entails that V redox centers are solely responsible for Na^+ exchange in the $Na_{3+y}V_{2-y}Mg_y(PO_4)_3$ cathodes, which enables us to follow structural and electrochemical (de)sodiation processes during charge-discharge more clearly than in the structurally and compositionally-similar V^{3+}-Mn^{2+} system. Specifically, this study allows us to evaluate the impact of metal mixing on the V site on the Na (de)intercalation mechanism, on the electrochemical reversibility, and on Na^+ diffusion kinetics, without the

complications of multi-metal redox processes on charge-discharge. We find that the progressive replacement of V^{3+} by Mg^{2+} in these Na-ion intercalation hosts provides a convenient handle for tuning their average intercalation voltage, voltage hysteresis and Na (de)intercalation mechanism.

2. RESULTS AND DISCUSSION

NASICON-$Na_{3+y}V_{2-y}Mg_y(PO_4)_3$ (y = 0, 0.25, 0.5, 0.75 and 1) cathodes were prepared *via* a sol-gel assisted high temperature method (see experimental section). Particle morphology of the as-prepared cathodes was studied using scanning electron microscopy (SEM) (Figure S1). The micrographs indicate the formation of micron-sized secondary particles composed of nanoscale primary particles, while CHN elemental analysis reveals the presence of 3-5 wt% carbon in the NASICON samples (Table S3).

X-ray diffraction (XRD) measurements were conducted to study the solubility of Mg^{2+} cations in the NVP framework (**Figure 1**a). All of the Bragg peaks observed for the $Na_{3+y}V_{2-y}Mg_y(PO_4)_3$ cathode samples can be fully indexed using a rhombohedral $R\bar{3}c$ space group, with no evidence of crystalline impurities. It is also worth noting that Inoishi *et al.*[11] highlighted the solubility limit of Mg^{2+} in the NVP lattice as y = 0.5, however, their sample preparation involved a high temperature annealing (800 ˚C) step that could lead to phase decomposition. To gain insights into long-range structural changes upon Mg^{2+} substitution, Rietveld refinements of the lab XRD data were carried out, and the results are displayed in Figures 1b, with structural parameters summarized in Table S4. Although NVP undergoes a

series of phase transitions upon cooling from the $R\bar{3}c$ form to a monoclinic *C2/c* structure near room temperature due to Na^+-ion/vacancy ordering,[34] herein its XRD pattern is refined using the rhombohedral $R\bar{3}c$ setting for the sake of comparison across the compositional series, and because the use of a C2/c structural model does not improve the refinement significantly. As the concentration of Mg^{2+} (*y*) increases from 0 to 1 in the NVP framework, we notice anisotropic changes to the lattice parameters along with an expansion of the unit cell volume ($\Delta a/a$ = +1.75 %, $\Delta c/c$ = -1.75 %, and $\Delta V/V$ = + 1.71 %). The decrease in the *c* lattice parameter with increasing *y* (from y = 0.25 to y = 1) can be related to the progressive filling of Na(1) sites, which minimizes the electrostatic repulsion between oxygen layers perpendicular to the *c*-axis of the NASICON structure. The larger ionic radius of Mg^{2+} ($r_{Mg^{2+}}$ = 0.72 Å), as compared to V^{3+} ($r_{V^{3+}}$= 0.64 Å), and the increase in Na(2) site population, are responsible for the increase in *a*-parameter. Further, BVS calculations reveal minor changes to the average (V/Mg)-O and Na(1)-O bond lengths, and reduced $(V/Mg)O_6$ and $Na(1)O_6$ octahedral distortions upon increased Mg^{2+} substitution (Table S4), which is also confirmed by X-ray absorption spectroscopy (XAS) results presented in the next section. When comparing these structural changes to those reported in our recent study of Mn^{2+} substitution into the NVP lattice,[21] we notice that $(V/Mg)O_6$ octahedra in $Na_{3+y}V_{2-y}Mg_y(PO_4)_3$ are less distorted (Δ = 2-3 $\times 10^{-4}$) than $(V/Mn)O_6$ octahedra in $Na_{3+y}V_{2-y}Mn_y(PO_4)_3$ (Δ = 5–7 $\times 10^{-4}$), which is presumably due to the different ionic sizes and bonding characteristics of Mg^{2+} and Mn^{2+}.

First principles calculations were carried out to confirm the phase stability and to evaluate the most favorable V/Mg ordering for the various $Na_{3+y}V_{2-y}Mg_y(PO_4)_3$ compositions of interest. For this, the formation energies of the solid solutions were computed using the following formula: $\Delta E_f = E_i - (y-3) \times E_{\text{¿¿}}$, where E_i is the total energy of the $Na_{3+y}V_{2-y}Mg_y(PO_4)_3$

composition under consideration, and $E_{¿¿}$ and $E_{¿¿}$ are the total energies of the end member phases. Starting from $Na_4VMg(PO_4)_3$ with a fully occupied Na sublattice, other compositions in the series were generated by removing Na-ions and adjusting the V^{3+}/Mg^{2+} ratio to maintain charge neutrality and achieve the targeted stoichiometries. Using the Supercell code, multiple V/Mg orderings were generated for each stoichiometry (see details in the SI). A convex hull plot was constructed using the formation energies of all of the converged $Na_{3+y}V_{2-y}Mg_y(PO_4)_3$ configurations and is shown in Figure S2a. The optimized lattice parameters for the most stable configurations are summarized in Table S5 and their evolution resemble our XRD results. We note here that no particular V and Mg ordering is observed for the lowest energy structures of $Na_{3+y}V_{2-y}Mg_y(PO_4)_3$, in good agreement with our experimental XRD results. We observe 3 types of local environments for Na(1) in the NASICON skeleton, namely, MgO_6-Na(1)O_6-MgO_6, VO_6-Na(1)O_6-MgO_6 and VO_6-Na(1)O_6-VO_6, wherein Na(1)O_6 polyhedra face share with MgO_6 /VO_6 octahedra. In the case of Na(2)O_8 polyhedra, these are found to be face sharing in MgO_6-Na(2)-MgO_6, VO_6-Na(2)-MgO_6 and VO_6-Na(2)-VO_6, and corner sharing in MgO_6-Na(2)-MgO_6 subunits. The calculations reveal that changing the local V/Mg ratio around Na species influences the energies of the configurations significantly, and thus plays a role in the preferred occupation of Na(1) and Na(2) sites across the $Na_{3+y}V_{2-y}Mg_y(PO_4)_3$ compositional series. In the lowest energy structures, both Na(1) and Na(2) prefer to occupy Mg-rich environments rather than mixed V/Mg and V-rich environments. The most stable configurations for the y = 0, 0.25, 0.5, 0.75 and 1 phases have a Na(1): Na(2) occupation ratio of 0.66:0.77, 0.75:0.83, 0.83:0.89, 0.91:0.94 and 0.94:0.99, respectively, and are considered hereafter.

To understand how Mg^{2+} substitution influences Na^+ ion mobility in the NASICON framework, Na^+ diffusion barriers (E_a) and bottleneck sizes (T1) obtained for the series of

$Na_{3+y}V_{2-y}Mg_y(PO_4)_3$ compositions are plotted in Figure S2b. The bottleneck area (T1) corresponds to the area of an isosceles triangle located in-between Na(1) and Na(2) sites. T1 values obtained from first principles calculations at each Mg^{2+} substitution agree fairly well with those obtained from Rietveld analysis. While a drop in T1 is observed at low substitution levels ($y \leq 0.25$), this is followed by a steady increase in T1 upon further Mg^{2+} substitution. Activation energies were obtained from CI-NEB calculations for sodium-ion hops between Na(1) to Na(2) sites through the T1 area. While E_a and T1 may naively be expected to be inversely related to one another, the trend in E_a is more complex upon increasing the Mg^{2+} content. Indeed, E_a increases from ~0.15 eV at $y = 0$ to ~0.38 eV at $y = 0.25$, and stabilizes at about 0.25 eV for $y = 0.5$ and 0.75 compositions, before increasing again to 0.5 eV in the fully sodiated compound ($y = 1$). This complex evolution is likely the result of the interplay between changes to the T1 bottleneck area and to Na site occupation on Mg^{2+} substitution.

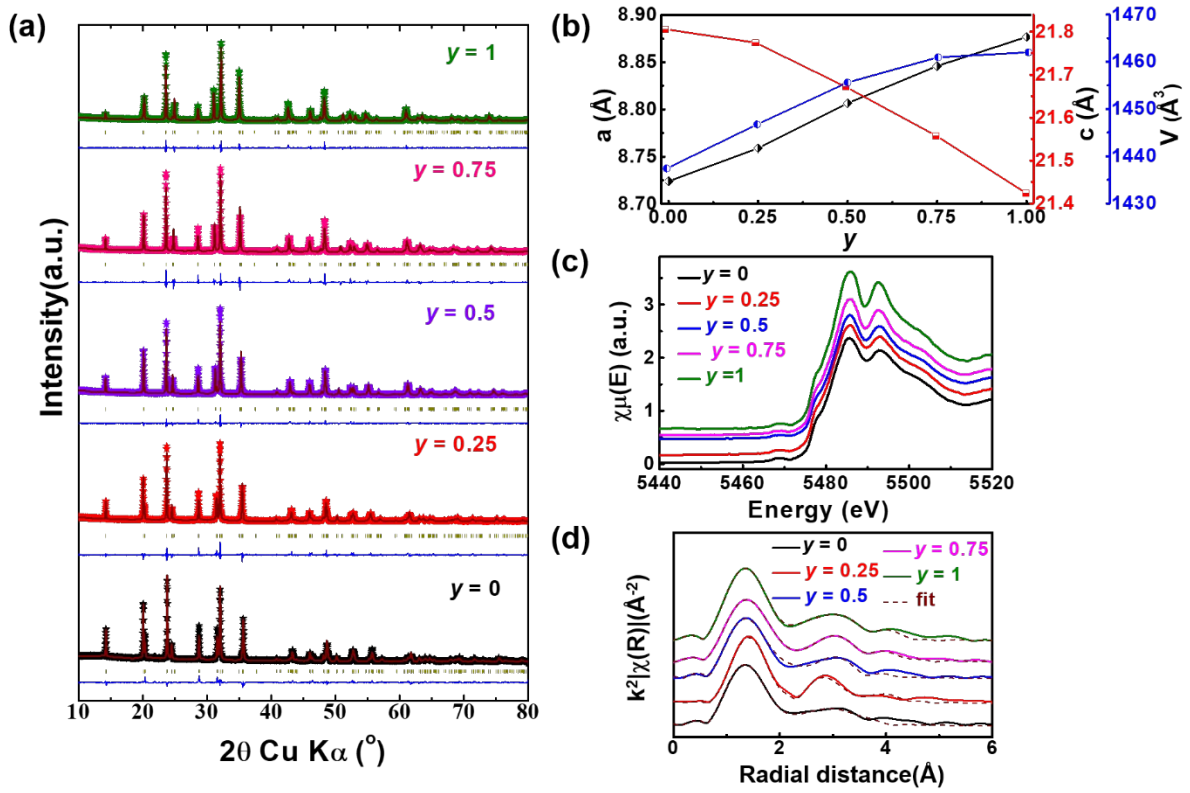

Figure 1. (a) Rietveld analysis of powder XRD patterns collected on $Na_{3+y}V_{2-y}Mg_y(PO_4)_3$ samples. (b) Variations in the unit cell parameters and volumes as a function of *y*. (c) Normalized absorption spectra and (d) FT-EXAFS at the V K-edge of the $Na_{3+y}V_{2-y}Mg_y(PO_4)_3$ cathodes.

XAS experiments were performed on as-synthesized $Na_{3+y}V_{2-y}Mg_y(PO_4)_3$ ($0 \leq y \leq 1$) samples to investigate potential changes in the vanadium oxidation state, as well as local structure changes across the series. Normalized V K-edge absorption spectra are shown in Figure 1c. Irrespective of the amount of Mg^{2+} substituted into the NVP framework, the position of the absorption edge is similar in all XAS spectra, confirming that the average V oxidation state is +3 in all samples. Magnitude plots of the Fourier-transformed extended X-ray absorption fine structure (FT-EXAFS) at the V K-edge, along with theoretical fits and extrapolated bond distances, are shown in Figure 1d and Table S6, respectively. We note that the FT-EXAFS data are not phase-corrected and peak positions do not reflect actual bond lengths. The first peak located at ~1.6 Å corresponds to scattering from V-O pairs, while the

next two peaks at ~2.8-3.2 Å are associated with V-P and V-Na outer shell correlations. Fits of the EXAFS spectra indicate a slight increase in the average V-O bond length on Mg^{2+} substitution, presumably due to reduced overlap between the V 3d orbitals and O 2p orbitals and enhanced bond ionicity. In contrast, the fits do not show any clear correlation between the evolution of the V-Na(1), V-P and V-Na(2) distances and the Mg^{2+} substitution level, yet significant changes are observed at each $\Delta y = 0.25$ step increase in Mg content. This may be explained by the concurrent increase in the total Na content and variations in the relative occupation of Na(1) and Na(2) sites upon Mg^{2+} substitution, resulting in a unique local structure for each composition.

^{23}Na and ^{31}P solid-state nuclear magnetic resonance (NMR) experiments were conducted to obtain further insights into local structure changes across the $Na_{3+y}V_{2-y}Mg_y(PO_4)_3$ series. The presence of open-shell V^{3+} species in these compounds results in strong hyperfine (or paramagnetic) interactions between unpaired electron spins nominally present in the V *3d* orbitals and the ^{23}Na / ^{31}P nuclear spins under study. These strong interactions result in significant NMR line broadening and potential signal overlap, complicating the assignment of the spectral features to specific local environments in the material. Furthermore, the isotropic chemical shift (δ_{iso}) is dominated by the Fermi contact shift resulting from delocalization of unpaired electron spin density from the V *3d* orbitals to the ^{23}Na (or ^{31}P) *s* orbitals via bridging O *2p* orbitals. For an $I = 3/2$ quadrupolar nucleus such as ^{23}Na, the interaction between the nuclear quadrupole moment and the electric field gradient (EFG) present at the nucleus leads to a further broadening of the spectrum and to a shift of the ^{23}Na resonant frequency due to second-order effects (denoted δ_Q). The observed chemical shift (δ_{obs}) is then the sum of the isotropic Fermi contact shift and of the second-order quadrupolar shift: $\delta_{obs} = \delta_{iso} + \delta_Q$. In contrast, ^{31}P is a spin-½ nucleus with no quadrupole moment and $\delta_{obs} = \delta_{iso}$. The

assignment of the complex paramagnetic NMR spectra of the $Na_{3+y}V_{2-y}Mg_y(PO_4)_3$ systems is assisted here by first principles hybrid DFT / Hartree Fock (HF) calculations of ^{23}Na and ^{31}P NMR parameters on the room temperature monoclinic (*C*2/*c* space group) and Na-ordered form of $Na_3V_2(PO_4)_3$ (α-$Na_3V_2(PO_4)_3$) identified by Chotard et al. [34]

^{23}Na spin echo NMR spectra obtained at 18.8 T are shown in **Figure 2**a. As expected from the reduced hyperfine interactions upon progressive replacement of paramagnetic V^{3+} by diamagnetic Mg^{2+}, a decrease in signal broadening is observed as *y* increases.[41] A shift of the average ^{23}Na resonant frequency towards 0 ppm is also observed on increasing the Mg^{2+} content, again, as expected from the reduced paramagnetism. To facilitate the interpretation of the high field ^{23}Na NMR data, additional spectra were collected at 7.05 T. Fits of the 7.05 and 18.8 T NMR data are shown in Figure S4 in the Supplementary Information. The observed chemical shifts (δ_{obs}) and relative integrated intensities of the various ^{23}Na resonances determined from fits of the NMR data are recorded in Table S7.

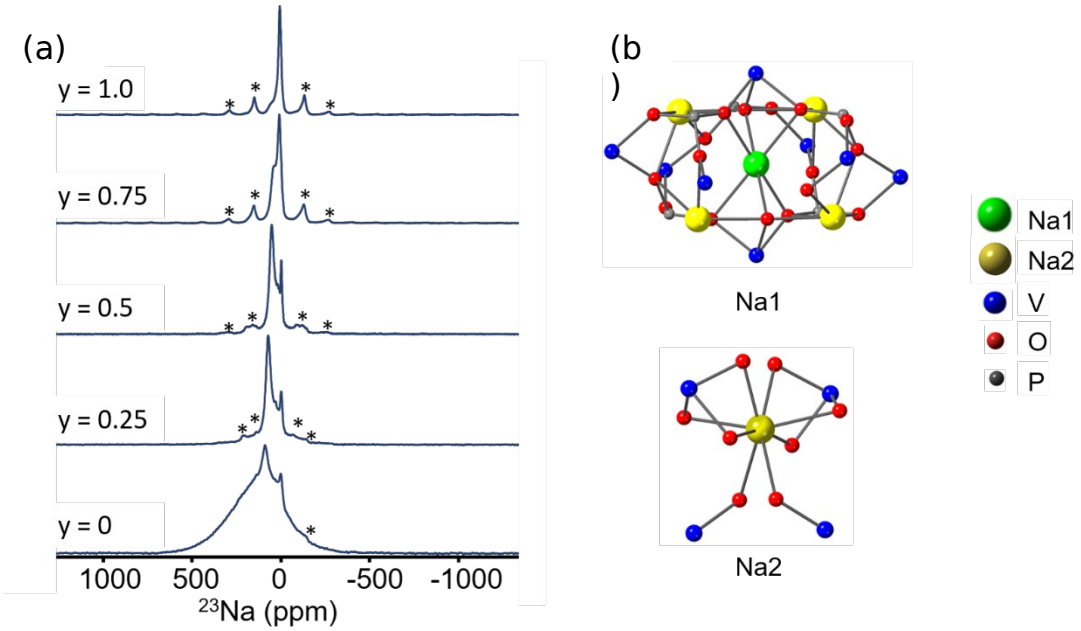

Figure 2. (a) ^{23}Na solid-state NMR spectra obtained on as-synthesized $Na_{3+y}V_{2-y}Mg_y(PO_4)_3$ at 18.8 T using a spin echo pulse sequence. (b) Local environments Na(1) (surrounded by 8 V

atoms) and Na(2) (surrounded by 4 V atoms) in the $Na_3V_2(PO_4)_3$ structure. Asterisks indicates spinning sidebands coming from the fast rotation of the sample during acquisition.

For the $y = 0$ composition, the two ^{23}Na resonances observed at $\delta_{obs} = 134$ ppm and $\delta_{obs} = 55$ ppm at 7.05 T (Figure S4a) can be attributed to Na^+ species in the NASICON structure, while the low intensity resonance near 0 ppm is attributed to (a) diamagnetic sodium phosphate and pyrophosphate impurity(ies).[42] ^{23}Na NMR parameters computed on the room temperature α-$Na_3V_2(PO_4)_3$[34] structure, where Na(1) sites split into Na(1a) and Na(1b) sites, and Na(2) sites split into Na(2a), Na(2b) and Na(2c) sites, are summarized in Table S8. A comparison of the observed (Table S7) and *ab-initio* predicted (Table S8) ^{23}Na chemical shifts indicates that the 134 and 55 ppm resonances are average signals due to fast Na^+ exchange *on the NMR timescale* between *subsets* of Na(1) and Na(2) environments in the α-NVP structure, rather than signals arising from the Na(1) and Na(2) crystallographic sites in the average rhombohedral (*R*3̄*c*¿ structural model. The NMR timescale denotes the ability of NMR to distinguish between different environments that are in chemical exchange and depends on the frequency separation ($\Delta\nu$, in Hz) between signals corresponding to the various environments in exchange. The presence of two distinct signals in the $y = 0$ spectrum indicates that room temperature Na-ion exchange between all Na sites in the NASICON structure is not sufficiently fast to result in a single average ^{23}Na resonance, but it is fast enough to average out signals with similar resonant frequencies. We attribute the 134 ppm resonance to an average signal arising from Na nuclei in Na(1a), Na(1b) and Na(2c) sites in the structure and associated with high (more positive) resonant frequencies. We further assign the 55 ppm resonance to an average signal due to Na nuclei in Na(2a), Na(2b) sites in the structure and associated with low (more negative) resonant frequencies. Moreover, the intensity ratio of the 134 and 55 pm signals of 1.21:1 is in much better agreement with partial averaging over Na(1a), Na(1b) and Na(2c) sites on the one hand, and over Na(2a) and Na(2b) sites on the

other hand (predicted 1.25:1 intensity ratio obtained from Na site multiplicities in the α-NVP structure), than over all Na(1) and all Na(2) sites (predicted 1:2 intensity ratio), as shown in Table S9. Based on the frequency difference (in Hz) between the 134 ppm and 55 ppm resonances in the low field (7.05 T) data, we estimate the exchange rate of Na^+ species between the high and low frequency resonances to be less than ≈ 12 kHz (i.e., the rate of exchange needed for these two ^{23}Na resonances to coalesce at the experimental temperature).

For the Mg-substituted samples, the assignment of the ^{23}Na NMR resonances (Figure S4) to specific sites in the NASICON structure is not straightforward. Assuming that Mg randomly substitutes on V sites, a large number of Na local environments are expected with varying numbers of Mg^{2+} species in the first metal coordination shell around Na(1) and Na(2) depicted in Figure 2b, resulting in a distribution of chemical shifts. For example, in the y = 0.5 sample, a total of 35 distinct Na(1) environments and 6 distinct Na(2) environments are expected. However, only two to three ^{23}Na resonances are observed in the NMR spectra collected on these phases (see Figure S4), suggesting that fast chemical exchange between subsets of Na(1) and Na(2) sites in these compounds results in ^{23}Na NMR signal averaging. Additionally, while we assign the sharp ^{23}Na resonance near 0 ppm in the y = 0.25 and 0.5 samples to diamagnetic sodium phosphate / pyrophosphate impurity(ies), the broader resonances in this frequency range in the y = 0.75 and 1 samples likely have contributions from Na sites in the paramagnetic NASICON cathode primarily surrounded by diamagnetic Mg^{2+} species.

^{31}P solid-state NMR experiments were conducted to monitor the evolution of the P local environments across the $Na_{3+y}V_{2-y}Mg_y(PO_4)_3$ series (**Figure 3**a). Spectral regions featuring paramagnetic ^{31}P NMR signals arising from the NASICON cathodes are shown in Figure 3a, and an example P local environment in NVP is provided in Figure 3b.

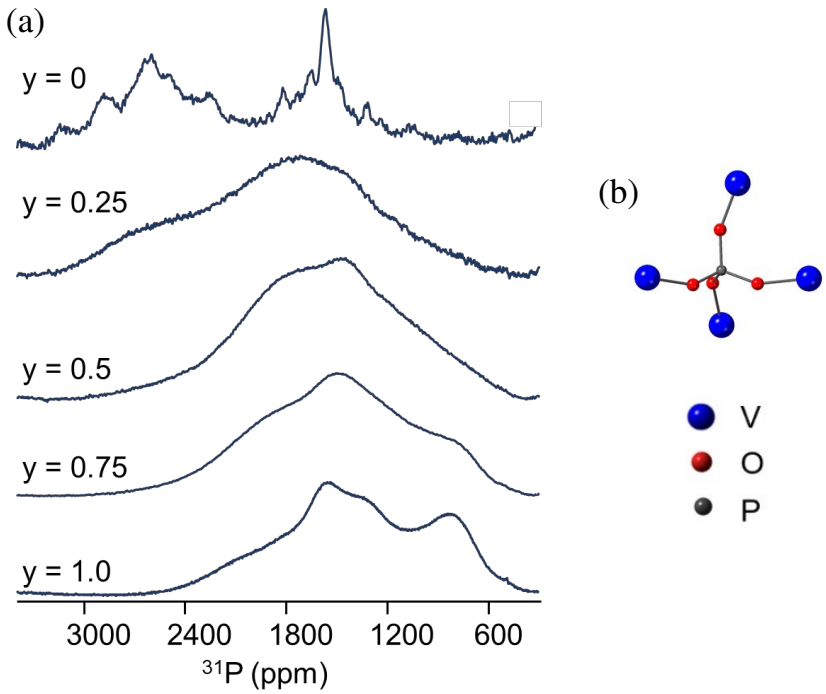

Figure 3. (a) Enlargements of the paramagnetic region of ^{31}P NMR spectra obtained on pristine $Na_{3+y}V_{2-y}Mg_y(PO_4)_3$ cathode samples at 7.05 T and at a spinning speed of 30 kHz. The full spectral window for each sample is shown in Figure S6. (b) Example P local environment in $Na_3V_2(PO_4)_3$.

As shown in Figure 3a, ^{31}P spectra collected on $Na_{3+y}V_{2-y}Mg_y(PO_4)_3$ pristine compounds are significantly broadened and feature multiple overlapping signals spanning a chemical shift range on the order of thousands of ppm. As the Mg dopant concentration is increased from y = 0.25 to y = 1, the reduced hyperfine interactions result in a decrease of the ^{31}P NMR signal broadening and concomitant shift of the resonant frequencies towards 0 ppm. For the y = 0 compound, we see multiple ^{31}P resonances suggesting the presence of multiple local ^{31}P environments in the material. This result is inconsistent with the rhombohedral ($R\bar{3}c$) model of $Na_3V_2(PO_4)_3$,[34] which contains a single P environment, and confirms the presence of a monoclinic structural distortion due to Na^+-ion/vacancy ordering close to room temperature.[34] The α-NVP structure comprises a total of five ^{31}P environments (PA, PB, PC, PD, and PE) that differ slightly in terms of P-O / O-V bond lengths and P-O-V bond angles (see Table

S10). The remarkable ^{31}P chemical shift range in the $y = 0$ spectrum, and the fact that all ^{31}P environments are similarly coordinated to four paramagnetic V^{3+} ions, as shown in Figure 3b, highlights the high sensitivity of ^{31}P shifts to even minor changes in the P local coordination. Although significant spectral overlap precludes a full assignment of the ^{31}P resonances, first principles calculations of ^{31}P NMR properties suggest that the PC and PE environments are responsible for the signals seen below 2000 ppm, and that resonances above 2000 ppm can be attributed to PA, PB, and PD environments (see Table S11).

Although paramagnetic interactions are reduced on Mg^{2+} substitution into $Na_{3+y}V_{2-y}Mg_y(PO_4)_3$, the $y = 0.25$ spectrum is broader than the $y = 0$ spectrum. The broader line shape can be accounted for by the presence of a broad distribution of chemical shifts reflecting a distribution of P local environments as Mg partially substitutes on the V sites. As the Mg concentration is increased beyond $y = 0.25$, the paramagnetic broadening is decreased but the distribution of ^{31}P environments is still present. Assuming a random substitution of V by Mg, we expect 16 distinct P environments in the rhombohedral ($R\bar{3}c$) Mg-substituted compounds; the probability of finding each of these 16 P sites depends on the exact Mg:V ratio. The presence of a large number of broad and overlapping signals makes the assignment of the ^{31}P spectra non-trivial, as shown in Figure S5 for the $y = 0.5$ spectrum.

Full ^{31}P NMR spectra (from -2000 to 4000 ppm) collected on all samples are shown in Figure S6, and exhibit additional resonances near 0 ppm attributed to diamagnetic phosphate / pyrophosphate impurities [43,44] and/or to ^{31}P sites in the NASICON structure surrounded by four diamagnetic Mg^{2+} ions. For instance, assuming a statistical distribution of V and Mg species in the $y = 1$ composition, the probability of finding a ^{31}P nucleus surrounded only by 4 Mg is 6.25%.

Having established how Mg^{2+} substitution for V^{3+} in $Na_{3+y}V_{2-y}Mg_y(PO_4)_3$ cathodes affects their (local) crystal structure and Na^+ ion diffusion properties, we move on to study their Na (de)intercalation properties through galvanostatic cycling at a C/10 rate in the voltage window of 3.8-2.75 V vs. Na^+/Na^0. The voltage-composition (x) profiles of the $Na_{3+y}V_{2-y}Mg_y(PO_4)_3$ cathodes from their second cycle are given in **Figure 4**a, and their cycling stability evaluated at C/10 rate, is shown in Figure 4b. Remarkably, all of the NASICON cathodes retain almost 99% of their initial discharge capacities at the end of 50th cycle. The $Na_3V_2(PO_4)_3$ cathode exhibits a flat charge/discharge profile with an average voltage of ~3.45 V vs. Na^+/Na^0, corresponding to the reversible exchange of 1.9 moles of Na *pfu*.[6,9] The large voltage plateau indicates that Na (de)intercalation proceeds *via* a two-phase reaction between the $Na_3V_2(PO_4)_3$ and $NaV_2(PO_4)_3$ end-member compositions. Compared to NVP, several changes in the electrochemical properties are observed as y increases: the amount of reversible Na exchange decreases (to 1.7, 1.43, 1.13 and 1.0 moles *pfu* for y = 0.25, 0.5, 0.75 and 1, respectively), the slope of the voltage-composition profiles increases, and the average

intercalation voltage increases.

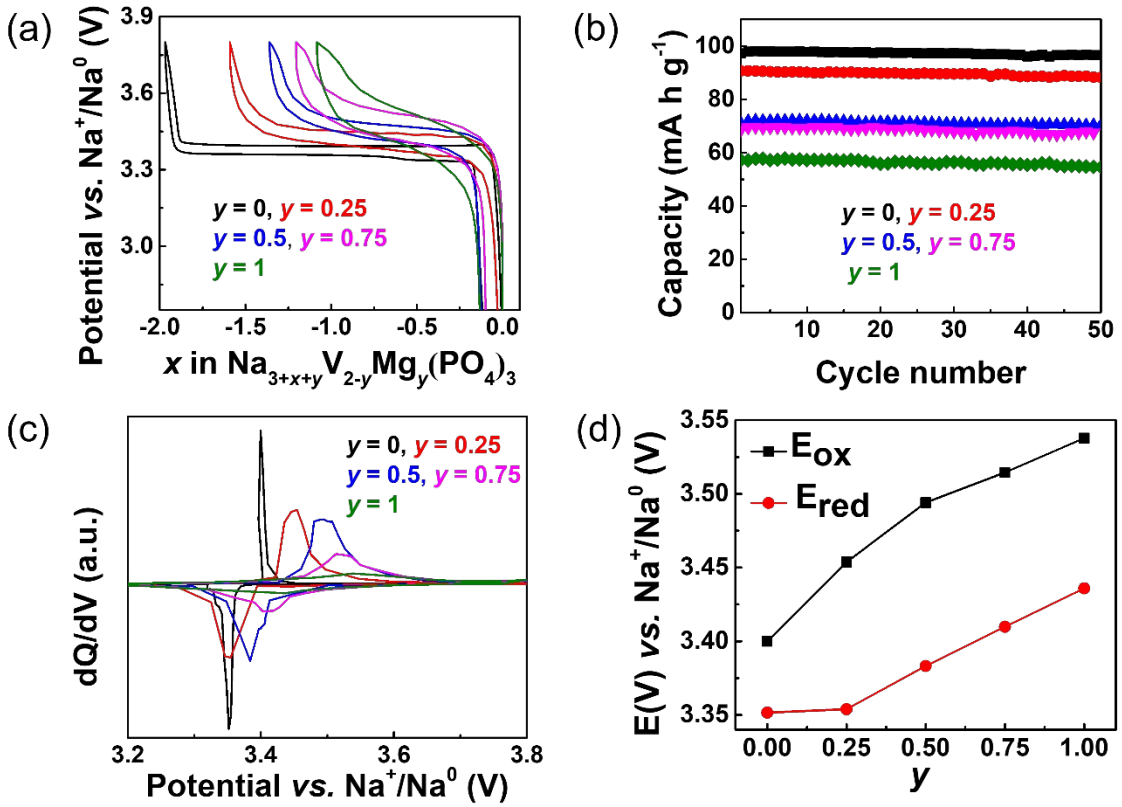

Figure 4. (a) Voltage vs. composition (x), (b) cycling performance, (c) dQ/dV profiles and (d) evolution of oxidation/reduction voltages (deduced from dQ/dV plots) of the $Na_{3+y}V_{2-y}Mg_y(PO_4)_3$ cathodes.

The decrease in the amount of cyclable Na (i.e., the charge storage capacity) with increasing y is related to the replacement of redox-active V^{3+} by electrochemically-inactive Mg^{2+} cations. The evolution of the average sodium (de)intercalation voltage and mechanism is best characterized *via* dQ/dV plots, as shown in Figure 4c and 4d. Changes to the average (de)intercalation potential (Figure 4d), from ~3.38 V at y = 0 to ~3.49 V at y = 1, can be attributed to variations in the V-O bonding character across the $Na_{3+y}V_{2-y}Mg_y(PO_4)_3$ series. Specifically, substitution of more electropositive Mg^{2+} ions for V^{3+} ions in the structure is expected to increase the ionicity of V-O bonds, thus raising the (de)intercalation voltage of the V^{4+}/V^{3+} redox couple. To confirm this, we computed the projected Density of States (pDOS) for all members of the $Na_{3+y}V_{2-y}Mg_y(PO_4)_3$ series (Figure S7a). We find that, while the valence states are majorly comprised by O-2p and Mg-2s orbitals, the V-3d orbitals dominate the higher energy conduction band states. The density of both V-3d and O-2p orbitals that are located near and below the Fermi level, respectively, decreases with increasing concentration of dopant Mg atoms, indicating a weakening of the hybridization between V and O orbitals due to the more polarizing nature of Mg^{2+}. This leads to a gradual reduction in the V-O bond covalency and to a lowering of the V-O* antibonding states, which in turn increases the V^{4+}/V^{3+} redox voltage. The pDOS results are confirmed by Bader charge analysis, which indicates an increase in the ionicity of V-O bonds and higher Bader charges on the V cations with increasing Mg content[45] (Figure S7b). The redox peaks in the dQ/dV plots in Figure 4c also become broader as y increases from 0 to 1, indicating a change in the Na (de)intercalation process upon Mg^{2+} substitution.-

To understand how Mg^{2+}substitution affects the Na (de)intercalation mechanism of the NVP cathode, we performed *in-operando* XRD studies on the y = 0.5 and 1 cathodes (**Figure 5**). Previous *in-operando* XRD studies on the unsubstituted NVP cathode have revealed a complete two-phase transformation mechanism between the $Na_3V_2(PO_4)_3$ and $NaV_2(PO_4)_3$ end-members, accompanied by the oxidation of V^{3+} to V^{4+}.[46] During the initial charge process, the XRD peaks of the $Na_{3.5}V_{1.5}Mg_{0.5}(PO_4)_3$ cathode progressively shift towards higher 2θ angles until 0.5 Na *pfu* has been extracted to form an intermediate $Na_3V_{1.5}Mg_{0.5}(PO_4)_3$, indicating a solid solution mechanism over this compositional range (Figure 5a). As the cathode is charged further, the XRD peaks of the $Na_3V_{1.5}Mg_{0.5}(PO_4)_3$ phase diminish whilst a new set of XRD peaks appears and grows at 2θ = 20.65° and 24.11°, confirming a first order phase transformation in this range. The XRD pattern collected at the end of charge (3.8 V) can be fitted with two NASICON phases (Figure 5b) and their corresponding lattice parameters are displayed in Table S12. The overall cell volume change between the Na-rich and Na-poor phases is estimated as 6.2 %, which is significantly lower compared to the NVP cathode (ΔV/V = 8.1 %). It is worth mentioning here that the presence of unextracted Na-ions in the Mg-substituted phases increases their volume and reduces the volume mismatch between Na-rich and Na-poor phases, resulting in enhanced structural integrity during cycling. Upon subsequent discharge, all of the processes observed on charge are reversed, and the XRD pattern collected at the end of the first cycle matches that of the pristine $Na_{3.5}V_{1.5}Mg_{0.5}(PO_4)_3$ cathode perfectly, thus confirming full reversibility of the Na (de)intercalation mechanism. In contrast, the fully sodiated $Na_4VMg(PO_4)_3$ cathode exhibits a solid solution mechanism over the entire Na (de)intercalation range (Figure 5c). Its XRD peaks shift towards higher and lower 2θ values during the charge and discharge process, respectively. The desodiated $Na_3VMg(PO_4)_3$ phase observed at 3.8 V shows anisotropic

lattice parameter changes (i.e., a decrease and an increase in the *a* and *c* lattice parameter, respectively) (see Figure 5d and Table S12). Importantly, we find that the occupancy of Na(1) and Na(2) sites decreases to 0.867 and 0.688, respectively, implying simultaneous Na extraction from both Na sites. This observation is in contrast with the desodiation processes of $Na_3V_2(PO_4)_3$ and $Na_4VMn(PO_4)_3$[17,47] cathodes wherein Na-ions from Na(1) site are not involved in the desodiation process until 3.8 V. Thus, it is clear that Mg-substitution affects the preference of sodium ion extraction from Na(1) and Na(2) sites, which could be due to the differences in site energies among the various local environments ($(V/Mg)O_6$-$(Na(1)O_6/Na(2)O_8)$-$(V/Mg)O_6$) as described in the earlier section. Detailed theoretical calculations are underway to decipher about it. Overall, the *in-operando* XRD results prove that the Na (de)intercalation mechanism of Mg-substituted $Na_{3+y}V_{2-y}Mg_y(PO_4)_3$ cathodes progressively changes from a two-phase process to a solid solution process as the Mg content increases in the NVP lattice. Similar behavior has also been noticed in the case of $Na_{3+y}V_{2-y}Mn_y(PO_4)_3$ cathodes.[48]

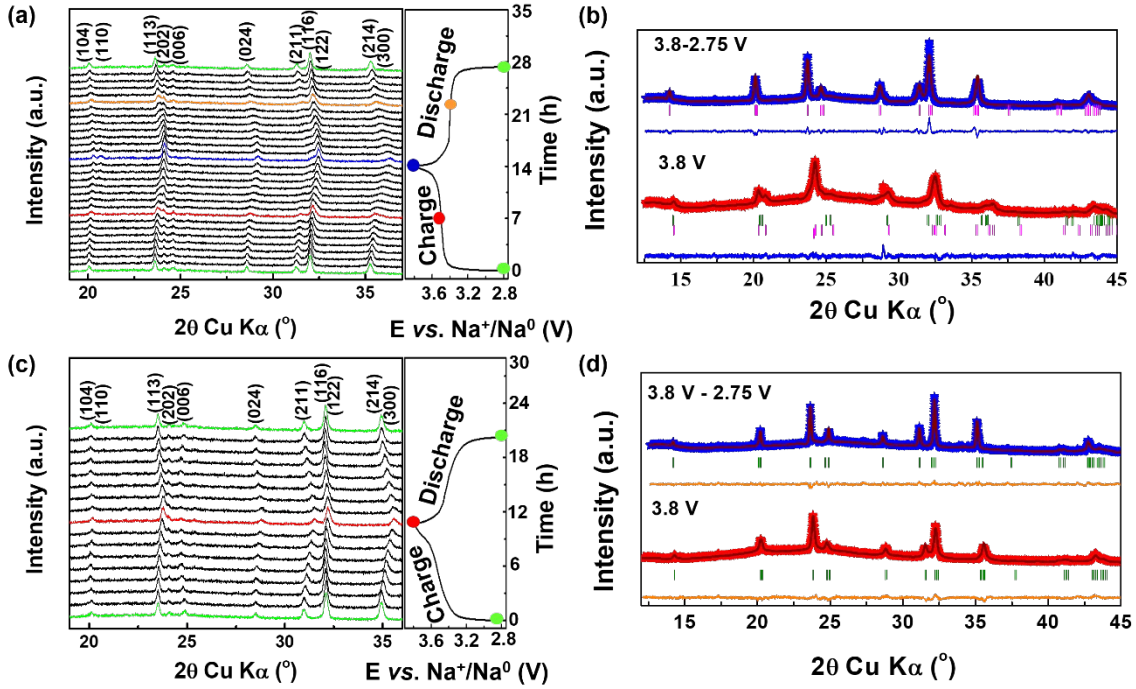

Figure 5. *In-operando* XRD (a, c) and *ex-situ* pattern refinements of (b, d) of y = 0.5 and 1 cathodes.

To understand the origin of the increased voltage polarization at higher Mg^{2+} substitution levels, GITT experiments were performed (**Figure 6**a and enlargements in Figure S8). We also recall here the theoretical calculation results presented earlier to correlate the Mg-substitution to the kinetic behaviors of the $Na_{3+y}V_{2-y}Mg_y(PO_4)_3$ cathodes. Although we cannot establish a direct correlation between the bottleneck sizes and the Na diffusion barrier (E_a), the latter increases for all of the Mg-substituted cathodes as compared to the NVP. Therefore, we expect an increase in the voltage hysteresis upon Mg substitution. However, we find that the charge-discharge voltage hysteresis initially decreases from y = 0 to y = 0.25 and 0.5, followed by an increase for the y = 0.75 and 1 compounds. The voltage-composition profiles obtained from GITT and galvanostatic cycling experiments are compared in Figure S9. For the y = 0.25 and 0.5 compositions, polarization is drastically reduced or completely vanishes when the voltage is allowed to relax to its equilibrium value (as in the GITT measurement), which is not the case for the y = 0.75 and 1 cathodes. The lowest polarization observed for y

= 0.5 cathode can be attributed to reduced lattice mismatch between the Na-rich and Na-poor end members of the two-phase reaction, as demonstrated by the *operando* XRD results. Such a phenomenon has been observed in, *e.g.*, related Li(Fe/Mn)PO_4 cathodes.[49-51] The impact of Mg-substitution on the Na (de)intercalation mechanism and kinetics is reflected in the rate performance of the $Na_{3+y}V_{2-y}Mg_y(PO_4)_3$, shown in Figure 6b. The y = 0.25, 0.5 & 0.75 cathodes deliver similar capacities as the y = 0 cathode at 1C and 2C rates, in contrast, the capacity of the y = 1 end member declines significantly at these high C-rates. These results highlight that two-phase Na (de)intercalation phenomena is not deleterious for high-rate performance and in fact lower voltage hysteresis can be achieved at intermediate Mg^{2+} substitution levels.

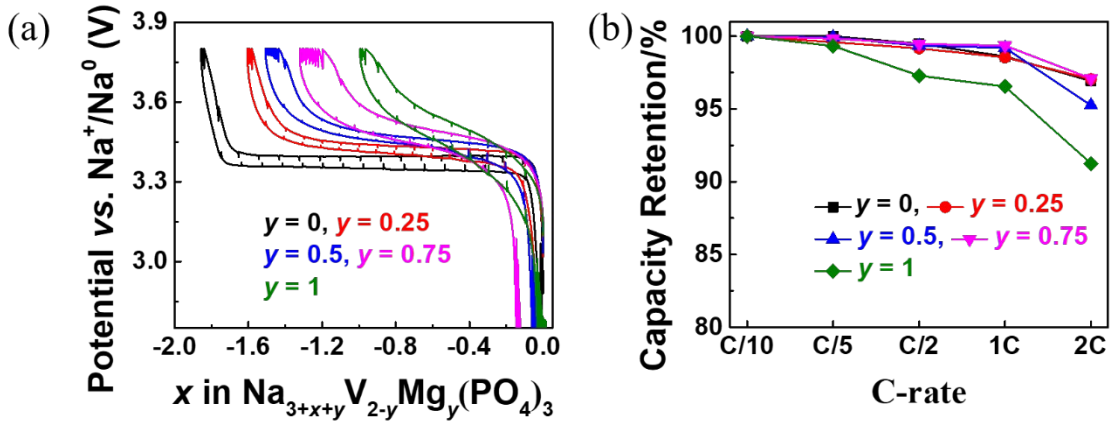

Figure 6. (a) GITT and (b) rate capability profiles of the $Na_{3+y}V_{2-y}Mg_y(PO_4)_3$ cathodes.

3. CONCLUSIONS

In this work, the impact of Mg^{2+} substitution on the structural and electrochemical Na (de)intercalation properties of $Na_{3+y}V_{2-y}Mg_y(PO_4)_3$ cathodes was investigated. Our combined XRD, XAS, NMR, and first principles results revealed a complex evolution of the (local) structure upon progressive replacement of V^{3+} by Mg^{2+}, along with the addition of Na ions into Na(1)/Na(2) sites, resulting in non-linear changes in the Na^+ diffusion properties across the compositional series. When cycled in the voltage window of 3.8-2.75 V, significant differences in the voltage-capacity profiles of the $Na_{3+y}V_{2-y}Mg_y(PO_4)_3$ cathodes were observed, including discrepancies in the average intercalation voltage, in the shape of the voltage curves and in their polarization. The increased Na insertion voltage on Mg substitution was attributed to more ionic V-O bond, as determined from pDOS and Bader charge analyses. A transition from a two-phase for $y \leq 0.5$ to a solid solution process on Na (de)intercalation for $y \geq 0.5$ was confirmed through *in-operando* XRD measurements. The lowest polarization value obtained for the $y = 0.5$ cathode was ascribed to minimized lattice mismatch between the Na-rich and Na-poor end members of the two-phase reaction. Further experimental and theoretical studies are in progress to understand the high voltage behavior of the $Na_{3+y}V_{2-y}Mg_y(PO_4)_3$ cathodes. Overall, the present work underlines the importance of tunning functionalities of cathodes and understanding their structure-property relationship upon cationic substitution to achieve high energy density NASICON cathodes.

4. EXPERIMENTAL

Synthesis: NASICON-$Na_{3+y}V_{2-y}Mg_y(PO_4)_3$ samples were synthesized using sol-gel method. Initially V_2O_5 (99.6%, Sigma) was reduced using citric acid (99.5%, Sigma) in water following addition of stoichiometric amount of NaH_2PO_4 (99%, Sigma), Na_2CO_3 (99.5%,

Sigma) and Mg-acetate (99%, Sigma) and the solution was subsequently heated at 100 °C to obtain powder mixture. The recovered powders were grinded using a mortar and pestle followed by annealing at 350 °C for 10 hours and 700 °C for 12 hours in N_2 atmosphere with an intermittent grinding.

Material Characterization: Powder X-ray diffraction (XRD) patterns of the $Na_{3+y}V_{2-y}Mg_y(PO_4)_3$ samples were collected on a Bruker D8 diffractometer using Cu-Kα source in the 2θ region of 10-100°. Rietveld analyses were performed to refine all the powder patterns using the FullProf program.[23] The as-synthesized phosphate cathode materials were examined by scanning electron microscope (Jeiss Ultra-55 SEM instrument) to get the microstructures. Carbon, hydrogen, and nitrogen (CHN) analysis was conducted on a Perkin–Elmer EA 2400 instrument.

X-ray absorption spectroscopic (XAS) studies of the as-synthesized NASICON compounds and the electrodes with different state-of-charge were performed at the PETRA-III (P65 beamline, operating at 100 mA and 7.0 GeV) of Deutsches Elektronen-Synchrotron (DESY). The NASICON samples were mixed with boron nitride and pressed into pellets (13 mm diameter, thickness 0.5-0.9 mm). For data collection purpose the electrodes at different charge states and the pellets were sealed in Kapton tape. The edge energy of 5349 eV was chosen for vanadium at the inflection point with the energy resolution of 1eV. Each measurement was calibrated to the absorption energy of V metal plate reference. A double crystal monochromator consistent of parallel Si (1 1 1) crystals was used for the measurement in transmission mode. Three consecutive ionization detectors, filled with gas mixtures of (first) 1250 mbar N_2, 750 mbar He; (second) 250 mbar Ar, 1000 mbar N_2, 750 mbar He; (third) 1000 mbar N_2, 300 mbar He, 700 mbar Ar, are at a pathlength of 30 cm. AutoBK

algorithm[24] as implemented in Athena and a graphical front-end for the IFFEFIT software package[25] were used for the normalization of data and removal of background.

Room temperature ^{23}Na and ^{31}P solid-state nuclear magnetic resonance (NMR) spectra were collected on $Na_{3+y}V_{2-y}Mg_y(PO_4)_3$ powder samples using a 7.05 T (300 MHz for ^{1}H) Bruker superwide bore NMR spectrometer equipped with an Avance III console and operating at Larmor frequencies of 79.39 MHz and 121.5 MHz, respectively. Additional ^{23}Na solid-state NMR experiments were performed at 18.8 T (800 MHz for ^{1}H) on a Bruker standard bore NMR spectrometer equipped with an Avance III console and operating at a Larmor frequency of 211.65 MHz. All NMR spectra were obtained under magic angle spinning (MAS) at a rate of 30 kHz using a 2.5 mm double-resonance HX probe. The ^{23}Na spectra were referenced against a 1M NaCl solution ($\delta(^{23}Na)$ = 0 ppm), and the ^{31}P spectra against a 1M H_3PO_4 solution ($\delta(^{31}P)$ = 0 ppm). Line shape analysis was carried out within the Bruker TopSpin software using the SOLA line shape simulation package. ^{23}Na and ^{31}P NMR spectra were recorded using a rotor-synchronized spin echo ($90° - \tau_R - 180° - \tau_R$ – acq). Low field (7.05 T) ^{23}Na spin echo were obtained using a 90° RF pulse of 0.8 μs and a 180° pulse of 1.6 μs at 300 W, with a recycle delay of 100 ms and averaged over 16,384 transients. High field (18.8 T) ^{23}Na NMR data were obtained using a 90° RF pulse of 0.97 μs and a 180° pulse of 1.94 μs at 200 W, with a recycle delay of 100 ms and averaged over 4,096 transients. Low field (7.05 T) ^{31}P spin echo spectra were obtained using a 90° RF pulse of 1.1 μs and a 180° pulse of 2.2 μs at 250 W, with a recycle delay of 100 ms. Further details on the analysis of the NMR results are provided in the Supplementary Information.

The field-cooled (FC) and zero field-cooled (ZFC) DC magnetic susceptibility of $Na_3V_2(PO_4)_3$ was recorded on a commercial magnetic property measurement system (MPMS)

over a 2-350 K temperature range. Measurements were performed under an external field of 1000 Oe.

Electrochemical Characterization: All electrochemical tests of the $Na_{3+y}V_{2-y}Mg_y(PO_4)_3$ cathodes were performed in two-electrode Swagelok cells. The cathode materials were mixed with carbon (C45 TIMCAL) and polyvinylidene fluoride (PVDF) binder in a weight ratio of 70:22:8 in N-Methyl-2-pyrrolidone solvent. The slurry was coated on aluminum foil and dried under vacuum at 90 °C for overnight. Thereafter, electrodes were punched into 10 mm diameter discs and the mass loading of active materials was found to be ~2.0 mg cm^{-2}. Sodium (Sigma, >99%) metal was used as the counter electrode and 1 M $NaClO_4$ in EC/PC/DMC (in a weight ratio of 4.5:4.5:0.1) with 3 wt% FEC was used as the electrolyte. The cells were assembled in an Ar-filled glovebox (O_2 < 0.1 ppm, H_2O < 0.1 ppm) and evaluated in a battery cycler (BT-lab, Biologic) over the voltage range 3.8-2.75 V vs. Na^+/Na^0 at different C-rates. For galvanostatic intermittent titration technique (GITT) experiments, a current equivalent to a C/10 rate was applied for 1 hour followed by a 4 hour relaxation. Prior to the GITT experiments, the cells were cycled at C/10 for three cycles.

In-operando XRD measurements were conducted using the same BRUKER D8 diffractometer with Cu-Kα source in an *in-situ* cell fitted with Be window. The cell was cycled at a C/10 rate in the voltage window of 3.8-2.75 V.

THEORETICAL CALCULATIONS

VASP Calculations: First Principles Density Functional Theory (DFT) calculations were performed using the PAW (Projector Augmented Plane Wave)[26] formalism as implemented in VASP[27-29] (Vienna Ab-Initio Simulation Package). The PBE[30] (Perdew-Burke-Ernzerhorf) functional under the Generalized Gradient Approximation (GGA) was used to

treat exchange and correlation effects. A Hubbard U correction term (U_V = 3.25 eV) was employed to treat electronic correlation in transition metal 3d orbitals, with the effective on-site exchange interaction parameter J fixed to 1 eV. A Kinetic Energy cutoff of 520 eV was used for PW expansion. The Brillouin Zone integration was performed using a 2x2x1 Monkhorst-Pack grid. All systems were optimized using the conjugate-gradient algorithm with a convergence criterion of 10^{-4} eV on energy 10^{-4} eV $Å^{-1}$ for residual forces. Crystal symmetry was preserved for all configurations.

A 2 x 1 x 6 supercell (with 252 atoms) was generated in order to achieve our target compositions across the $Na_{3+y}V_{2-y}Mg_y(PO_4)_3$ series, and study local environments and possible Na^+ occupancies. The Supercell[31] code was utilized to generate multiple configurations with a stochastic distribution of V^{3+} and Mg^{2+} for the entire series. Na^+/vacancy configurations with the lowest computed electronic energy were retained for further calculations. These configurations were then geometry optimized, with an energy convergence criterion of 10^{-4} eV/Å for residual forces on the atoms, and the lowest energy ordering was determined (for more details, see SI).

Bader charge analysis was performed using a code developed by Henkelman *et al.*[32] to determine the evolution of atomic charges and V-O bonding across the compositional series.

The Climbing-Image Nudged Elastic Band (CI-NEB)[33] method was utilized to determine activation barriers for Na ion hopping. For single ion hops, a path was interpolated from a filled Na site to the nearest vacant Na site.

Crystal calculations: Hybrid density functional theory (DFT) / Hartree Fock (HF) calculations were performed in the spin-unrestricted approach to determine ^{23}Na and ^{31}P NMR parameters in monoclinic α-$Na_3V_2(PO_4)_3$, the sodium-ordered form of $Na_3V_2(PO_4)_3$

(*C*2/*c* space group) determined by Chotard et al.[34] to be stable below ~25.8°C using single crystal X-ray diffraction. NMR calculations were carried out on *ab initio* optimized structures, with full optimization of the atomic positions and cell parameters. The CRYSTAL17 all-electron linear combination of atomic orbital code was used,[35,36] and two spin-polarized exchange-correlation functionals based on the B3LYP form[37-40] were applied, with Fock exchange weights of F_0 = 20 % (B3LYP or H20) and 35 % (H35). Full details of the hybrid DFT calculations, including basis sets, numerical parameters, and the procedure for scaling the computed NMR parameters to compare with experimental results, are presented in the SI.

Supporting Information

Supporting Information is available from the Wiley Online Library or from the author.

Acknowledgements

This work was supported by Department of Science & Technology (DST), Government of India (DST/TMD/MES/2K18/188) and Sheikh Saqr Laboratory, JNCASR. The authors acknowledge DESY (Hamburg, Germany), a member of the Helmholtz Association HGF, for the provision of experimental facilities. Parts of this research were carried out at PETRA III and the authors thank Dr. Edmund Welter for his assistance in using Beamline P65, and DST for financial assistance for the measurement at DESY. The NMR results reported here made use of the shared facilities of the Materials Research Science and Engineering Center (MRSEC; NSF DMR-1720256) at UC Santa Barbara, a member of the Materials Research Facilities Network (www.mrfn.org). Use was made of computational facilities purchased with funds from the National Science Foundation (CNS-1725797) and administered by the Center for Scientific Computing (CSC). The CSC is supported by the California NanoSystems Institute and the MRSEC (NSF DMR-1720256) at UC Santa Barbara. E. Gonzalez-Correa was supported by the NSF Graduate Research Fellowship Program (NSF DGE-1650114), and by the NSF Louis Stokes Alliance for Minority Participation (LSAMP) program (NSF HRD-1701365). A. Zaveri was supported by the MRSEC-sponsored Research Interns in Science and Engineering (RISE) and Future Leaders in Advanced Materials (FLAM) programs under (NSF DMR-1720256). SKP acknowledges JC Bose Fellowship, SERB, DST, Govt. of India for support.

Conflict of Interest

The authors declare no conflict of interest.

Author Contributions

‖S.G. and N.B. have contributed equally to this manuscript. All authors have given approval to the final version of the manuscript.

Keywords

Sodium-ion batteries, NASICON cathodes, Mg substitution.

Author Information

Corresponding Author

*E-mail: prem@jncasr.ac.in and rclement@ucsb.edu

ORCID

Premkumar Senguttuvan: 0000-0001-8465-5896.

Raphaële Clément: 0000-0002-3611-1162.

Referrences

[1] Z. Yang, J. Zhang, M. C. W. Kintner-Meyer, X. Lu, D. Choi, J. P. Lemmon, J. Liu, *Chem. Rev*. **2011**, *111*, 3577.

[2] J-Y. Hwang, S-T. Myung, Y-K. Sun, *Chem. Soc. Rev*. **2017**, *46*, 3529.

[3] S. Chen, C. Wu, L. Shen, C. Zhu, Y. Huang, K. Xi, J. Maier, Y. Yu, *Adv. Mater* **2017**, *29*, 1700431.

[4] J. B. Goodenough, H. Y-P. Hong, J. A. Kafalas, *Mater. Res. Bull*. **1976**, *11*, 203.

[5] C. Delmas, F. Cherkaoui, A. Nadiri, P. Hagenmuller, *Mater. Res. Bull.* **1987**, *22*, 631.

[6] S. Y. Lim, H. Kim, R. A. Shakoor, Y. Jung, J. W. Choi, *J. Electrochem. Soc.* **2012**, *159*, A1393.

[7] K. Kawai, W. Zhao, S-i. Nishimura, A. Yamada, *ACS Appl. Energy Mater.* **2018**, *1*, 928.

[8] R. Rajagopalan, B. Chen, Z. Zhang, X-L. Wu, Y. Du, Y. Huang, B. Li, Y. Zong, J. Wang, G-H. Nam, M. Sindoro, S. X. Dou, H. K. Liu, H. Zhang, *Adv. Mater* **2017**, *29,* 1605694.

[9] W. Song, X. Ji, Z. Wu, Y. Zhu, Y. Yang, J. Chen, M. Jing, F. Li, C. E. Banks, *J. Mater. Chem. A* **2014**, *2*, 5358.

[10] M. J. Aragón, P. Lavela, G. F. Ortiz, J. L. Tirado, *ChemElectroChem*. **2015**, *2*, 995.

[11] A. Inoishi, Y. Yoshioka, L. Zhao, A. Kitajou, S. Okada, *ChemElectroChem*. **2017**, *4*, 2755.

[12] H. Li, H. Tang, C. Ma, Y. Bai, J. Alvarado, B. Radhakrishnan, S. P. Ong, F. Wua, Y. S. Meng, C. Wu, *Chem. Mater.* **2018**, *30*, 2498.

[13] W. Shen, H. Li, Z. Guo, Z. Li, Q. Xu, H. Liu, Y. Wang, *RSC Adv*. **2016**, *6*, 71581.

[14] F. Lalère, V. Seznec, M. Courty, R. David, J. N. Chotard, C. Masquelier, *J. Mater. Chem. A* **2015**, *3*, 16198.

[15] R. Liu, G. Xu, Q. Li, S. Zheng, G. Zheng, Z. Gong, Y. Li, E. Kruskop, R. Fu, Z. Chen, K. Amine, Y. Yang, *ACS Appl. Mater. Interfaces* **2017**, *9*, 43632.

[16] Y. Zhao, X. Gao, H. Gao, H. Jin, J. B. Goodenough, *Adv. Funct. Mater*. **2020**, *30*, 1908680.

[17] W. Zhou, L. Xue, X. Lü, H. Gao, Y. Li, S. Xin, G. Fu, Z. Cui, Y. Zhu, J. B. Goodenough, *Nano Lett*. **2016**, *16*, 7836.

[18] F. Chen, V. M. Kovrugin, R. David, O. Mentré, F. Fauth, J. N. Chotard, C. Masquelier, *Small Methods* **2019**, *3*, 1800218.

[19] M. V. Zakharkin, O. A. Drozhzhin, I. V. Tereshchenko, D. Chernyshov, A. M. Abakumov, E. V. Antipov, K. J. Stevenson, *ACS Appl. Energy Mater.* **2018**, *1*, 5842.

[20] R. Liu, S. Zheng, Y. Yuan, P. Yu, Z. Liang, W. Zhao, R. Shahbazian-Yassar, J. Ding, J. Lu, Y. Yang, *Adv. Energy Mater*. **2021**, *11*, 2003256.

[21] S. Ghosh, N. Barman, M. Mazumder, S. K. Pati, G. Rousse, P. Senguttuvan, *Adv. Energy Mater*. **2020**, *10*, 1902918.

[22] D. V. Anishchenko, M. V. Zakharkin, V. A. Nikitina, J. Keith; K. J. Stevenson, E. V. Antipov, *Electrochim. Acta* **2020**, *354*, 136761.

[23] J. R. Carvajal, *Phys. B* **1993**, *192*, 55.

[24] M. Newville, *Synchrotron Rad.* **2001**, *8*, 322.

[25] B. Ravel, M. Newville, *J. Synchrotron Rad.* **2005**, *12*, 537.

[26] G. Kresse, D. Joubert, *Phys. Rev. B: Condens. Matter Mater. Phys.* **1999**, *59*, 1758–1775.

[27] G. Kresse, J. Hafner, *Phys. Rev. B* **1993**, *47*, 558.

[28] G. Kresse, J. Furthmüller, *Computational Materials Science* **1996**, *6*, 15.

[29] G. Kresse, J. Furthmüller, *Phys. Rev. B* **1996**, *54*, 11169.

[30] J. P. Perdew, K. Burke, M. Ernzerhof, *Phys. Rev. Lett*. **1996**, *77*, 3865.

[31] K. Okhotnikov, T. Charpentier, S. Cadars, *J. Cheminform*. **2016**, *8*, 17.

[32] W. Tang, E. Sanville, G. Henkelman, *Journal of Physics: Condensed Matter* **2009**, *21*, 084204.

[33] G. Henkelman, B. P. Uberuaga, H. Jonsson, *J. Chem. Phys*. **2000**, *113*, 9901.

[34] J-N. Chotard, G. Rousse, R. David, O. Mentré, M. Courty, C. Masquelier, *Chem. Mater.* **2015**, *27*, 5982.

[35] R. Dovesi, V. R. Saunders, C. Roetti, R. Orlando, C. M. Zicovich-Wilson, F. Pascale, B. Civalleri, K. Doll, N. M. Harrison, I. J. Bush, P. D'Arco, M. Llunell, M. Causà, Y. Noël, L.

Maschio, A. Erba, M. Rerat, S. Casassa, CRYSTAL17 User's Manual (University of Torino, Torino, **2017**).

[36] R. Dovesi, A. Erba, R. Orlando, C. M. Zicovich-Wilson, B. Civalleri, L. Maschio, M. Rérat, S. Casassa, J. Baima, S. Salustro, B. Kirtman, *WIREs Comput Mol Sci.* **2018**, *8*, e1360.

[37] A. D. Becke, *J. Chem. Phys.* **1993**, *98*, 5648.

[38] C. Lee, W. Yang, R. Parr, *Phys. Rev., B Condens. Matter* **1988**, *37*, 785.

[39] S. H. Vosko, L. Wilk, M. Nusair, *Can. J. Phys.* **1980**, *58*, 1200.

[40] P. J. Stephens, F. J. Devlin, C. F. Chabalowski, M. J. Frisch, *J. Phys. Chem.* **1994**, *98*, 11623.

[41] R. G. Shulman, *J. Chem. Phys.* **1958**, *29*, 945.

[42] K. H. Lim, C. P. Grey, *Solid State Nucl Magn Reson*. **1998**, *13*(1-2):101.

[43] D. Liu, X. Li, L. Wei, T. Zhang, A. Wang, C. Liu, R. Prins, *Dalton Trans*. **2017**, *46*, 6366.

[44] P. Conte, D. Šmejkalová, A. Piccolo, R. Spaccini, *Eur. J. Soil Sci.* **2008**, *59*, 584.

[45] B. C. Melot, D. O. Scanlon, M. Reynaud, G. Rousse, J-N. Chotard, M. Henry, J-M. Tarascon, *ACS Appl. Mater. Interfaces* **2014**, *6*, 10832.

[46] Z. Jian, W. Han, X. Lu, H. Yang, Y-S. Hu, J. Zhou, Z. Zhou, J. Li, W. Chen, D. Chen, L. Chen, *Adv. Energy Mater*. **2013**, *3*, 156.

[47] Z. Jian, C. Yuan, W. Han, X. Lu, L. Gu, X. Xi, Y.-S. Hu, H. Li, W. Chen, D. Chen, Y. Ikuhara, L. Chen, *Adv. Funct. Mater*. **2014**, *24*, 4265.

[48] M. V. Zakharkin, O. A. Drozhzhin, S. V. Ryazantsev, D. Chernyshov, M. A. Kirsanova, I. V. Mikheev, E. M. Pazhetnov, E. V. Antipov, K. J. Stevenson, *Journal of Power Sources*, **2020**, *470*, 228231.

[49] F. Omenya, N. A. Chernova, R. Zhang, J. Fang, Y. Huang, F. Cohen, N. Dobrzynski, S. Senanayake, W. Xu, M. S. Whittingham, *Chem. Mater.* **2013**, *25*, 85.

[50] G. Chen, A. K. Shukla, X. Song, T. J. Richardson, *J. Mater. Chem.*, **2011**, *21*, 10126-10133.

[51] F. Omenya, B. Wen, J. Fang, R. Zhang, Q. Wang, N. A. Chernova, J. Schneider-Haefner, F. Cosandey, M. S. Whittingham, *Adv. Energy Mater*. **2015**, *5*, 1401204.

TOC

NASICON-$Na_{3+y}V_{2-y}Mg_y(PO_4)_3$

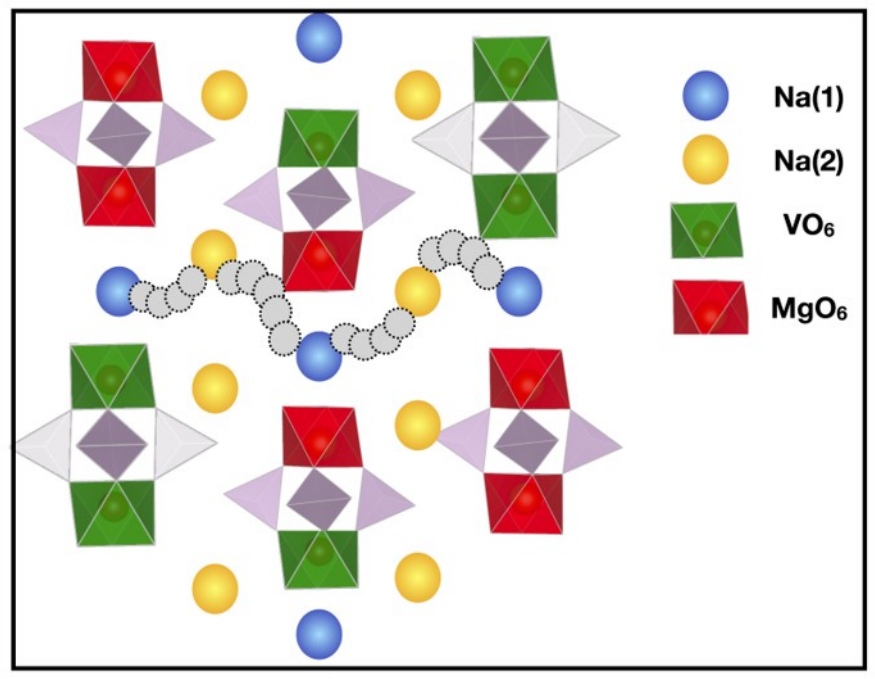

0 ≤ y ≤ 1: Change in Na-ion diffusion and (de)intercalation mechanism

Supplementary Information

Elucidating the Impact of Mg Substitution on the Properties of NASICON $Na_{3+y}V_{2-y}Mg_y(PO_4)_3$ Cathodes

Subham Ghosh,[‖,a,b,c,] Nabadyuti Barman,[‖,a,b,c] Eliovardo Gonzalez-Correa,[d,e] Madhulika Mazumder,[a,c,f] Aryan Zaveri,[e,g] Raynald Giovine,[d,e] Alexis Manche,[d,h,#] Swapan K. Pati,[c,f] Raphaële J. Clément,[d,e,] and Premkumar Senguttuvan [a,b,c,*]*

[a]New Chemistry Unit, [b]International Centre for Materials Science and [c]School of Advanced Materials, Jawaharlal Nehru Centre for Advanced Scientific Research, Jakkur, Bangalore-560064, India.

[d]Materials Department, University of California Santa Barbara, Santa Barbara, CA 93106-5050, USA.

[e]Materials Research Laboratory, University of California Santa Barbara, Santa Barbara, CA 93106-9530, USA.

[f]Theoretical Science Unit, Jawaharlal Nehru Centre for Advanced Scientific Research, Jakkur, Bangalore-560064, India.

[g]Physics Department, University of California Santa Barbara, Santa Barbara, CA 93106-9530, USA.

[h]Université de Bordeaux, UF Chimie, F-33405, Talence, France.

[#]Present address: School of Chemistry, University of St Andrews, North Haugh, St Andrews, KY16 9ST, United Kingdom.

Corresponding author

prem@jncasr.ac.in

rclement@ucsb.edu.

Additional details on structural enumeration and DFT calculations

Before proceeding with electronic structure calculations, we generated all possible configurations of the $Na_{3+y}V_{2-y}Mg_y(PO_4)_3$ series using the Supercell code to identify the most stable arrangement of V/Mg species and most favorable distribution of Na amongst Na(1) and Na(2) lattice sites.

Firstly, the crystal structure of $Na_4VMg(PO_4)_3$ obtained from Rietveld analysis was used in a 2x1x3 conventional cell (containing 6 formula units) configuration to generate multiple random orderings of V/Mg and Na(1/)Na(2). Because Supercell uses the special quasirandom structures (SQS) approximation, this procedure generated 924 random prototypical disordered structures. We identified 100 symmetrically-unique structures by visual inspection using the VESTA software package. Structures with minor differences were disregarded to keep computational costs tractable. The lowest energy configuration was identified after geometry optimization of these symmetrically-unique structures.

Thereafter, we replicated the $Na_4VMg(PO_4)_3$ conventional cell twice along the *c* axis, generating a 2x1x6 supercell in the process. This large supercell (12 formula units) allowed for intermediate compositions within the $Na_{3+y}V_{2-y}Mg_y(PO_4)_3$ series to be generated by removing stoichiometric amounts of Na(1) and Na(2), while changing the V/Mg ratio. A similar procedure as the one employed for $Na_4VMg(PO_4)_3$ was followed to obtain symmetrically-unique optimized structures for all of the compositions of interest. The number of structures generated by the Supercell code and the number of symmetrically-unique structures used as a starting point for DFT calculations are listed in Table S1. The ground state V/Mg and Na1/Na2 configuration for each $Na_{3+y}V_{2-y}Mg_y(PO_4)_3$ composition corresponds to the structure with the lowest formation energy after structural relaxation, as shown with the convex hull in Figure S2.

CRYSTAL17 calculations of paramagnetic NMR parameters

Computational details

Spin-unrestricted hybrid density functional theory (DFT) / Hartree Fock (HF) calculations were performed using the CRYSTAL17 all-electron linear combination of atomic orbital code[1,2] to determine ^{23}Na and ^{31}P NMR parameters in α-$Na_3V_2(PO_4)_3$ (α-NVP).

Two spin-polarized exchange-correlation functionals based upon the B3LYP form,[3-6] and with Fock exchange weights of F_0 = 20 % (H20) and 35 % (H35) were chosen for their good

performance for the electronic structure and band gaps of transition metal compounds[7,8] (H20), and for their accurate description of the magnetic properties of related compounds[9-11] (H35). Besides, previous studies have shown that the hyperfine shifts calculated with the H20 and the H35 functionals on similar compounds are in good agreement with experiment.[12-14]

All-electron atom-centered basis sets comprising fixed contractions of Gaussian primitive functions were employed throughout. Two types of basis sets were used: a smaller basis set (BS-I) was employed for structural optimizations, and a larger basis set (BS-II) was used for computing ^{23}Na and ^{31}P NMR parameters which require an accurate description of the occupation of core-like electronic states. For BS-I, individual atomic sets are of the form (15s7p)/[1s3sp] for Na, (20s12p4d)/[1s4sp2d] for V, (14s6p1d)/[1s3sp1d] for O, and (16s8p1d)/[1s3sp1d] for P where the values in parentheses denote the number of Gaussian primitives and the values in square brackets the contraction scheme. All BS–I sets were obtained from the CRYSTAL online repository and were unmodified from their previous use in a broad range of compounds.[1] For BS-II, modified IGLO-III (10s6p2d)/[6s5p2d] and (11s7p3d)/[7s6p3d] sets were adopted for O and P, respectively, a flexible and extended TZDP-derived (11s7p)/[7s3p] set was used for Na, and an Ahlrichs DZP-derived[15] (13s9p5d)/[7s5p3d] was adopted for V. The O and P BS–II sets are consistent with those used in a recent study on lithium transition metal phosphates.[14]

NMR parameters were computed on the fully optimized (atomic positions and cell parameters) α-NVP structure proposed by Chotard et al.[16] All first principles structural optimizations were carried out in the ferromagnetic (FM) state, after removal of all symmetry constraints (within the P1 space group) and using the H20 and H35 hybrid functionals. The 240 atom cell proposed by Chotard et al.[16] was used throughout. Structural optimizations were pursued using the quasi-Newton algorithm with RMS convergence tolerances of 10^{-7}, 0.0003, and 0.0012 au for total energy, root-mean-square (rms) force, and rms displacement, respectively. Tolerances for maximum force and displacement components were set to 1.5 times the respective rms values. Sufficient convergence in total energies and spin densities was obtained by application of integral series truncation thresholds of 10^{-7}, 10^{-7}, 10^{-7}, 10^{-7}, and 10^{-14} for Coulomb overlap and penetration, exchange overlap, and g- and n-series exchange penetration, respectively, as defined in the CRYSTAL17 documentation.[1] The final total energies and spin and charge distributions were obtained in the absence of any spin and

eigenvalue constraints. NMR parameters were obtained on ferromagnetically aligned supercells, and on supercells in which one V spin was flipped, using BS-II sets and a method identical to that described in Middlemiss et al.'s work.[13] Anisotropic Monkhorst-Pack reciprocal space meshes[17] with shrinking factors 6 9 3 were used for both H20 and H35 calculations. The lattice parameters for the α-NVP structures relaxed using the H20 and H35 functionals are compared to the experimental (EXP) unit cell parameters[16] in Table S2.

Comparing first principles (CRYSTAL17) and experimental NMR parameters

The computed hyperfine (paramagnetic) NMR properties are obtained at 0 K for NVP supercells containing ferromagnetically-aligned open-shell V^{3+} ions. To compare CRYSTAL17 calculation results with experimental data acquired at room temperature, the computed shifts must be subsequently scaled to a value consistent with the paramagnetic state of the system at the temperature of the NMR experiments, using a magnetic scaling factor Φ of the form:

$$\Phi(T_{\mathrm{exp}}) = \frac{\langle M(T_{\mathrm{exp}}) \rangle}{M_{sat}}, \qquad (1)$$

where M_{sat} is the saturated (ferromagnetic) V^{3+} magnetic moment at 0 K, and $\langle M(T_{\mathrm{exp}}) \rangle$ the bulk average magnetic moment measured at the sample experimental temperature, T_{exp}. Here, T_{exp} is set to 310 K to account for frictional heating caused by fast (30 kHz) sample rotation during NMR data acquisition.

The magnetic scaling factor in eq. (1) can be evaluated from the experimental magnetic properties of the material:

$$\Phi(T) = \frac{B_0 \mu_{eff}^{\ 2}}{3 k_B g_e \mu_B S(T - \Theta)}, \qquad (2)$$

where B_0 is the external magnetic field, μ_{eff} is the effective magnetic moment per V site, k_B is Boltzmann's constant, g_e is the free electron g-value, μ_B is the Bohr magneton, S is the formal spin of V^{3+} (d^2, $S = 1$ ¿, and Θ is the Weiss constant. A derivation of eq. (2), starting from the Brillouin function in the low field, high temperature limit, can be found in a previous study by Kim et al.[12] Eq. (2) uses the 'spin-only' expression for the magnetic moment and is only strictly valid when the orbital angular momentum is quenched.[18] Yet, for systems where spin orbit coupling effects are negligible, such as NVP, the spin-only

expression is a good approximation to the true magnetic behavior of the system. The experimental inverse magnetic susceptibility vs. temperature curve obtained for NVP is shown in Figure S3. From these data, an effective magnetic moment per V site $\mu_{eff} = 3.77\,\mu_B$ and a Weiss temperature $\Theta = -54.75$ K are obtained. A bulk magnetic scaling factor $\Phi = 0.030755$, is obtained for T = 310 K and $B_0 =$ ¿7.05 T. This value was used to scale the computed ^{23}Na and ^{31}P NMR parameters listed in Tables S7 and S9.

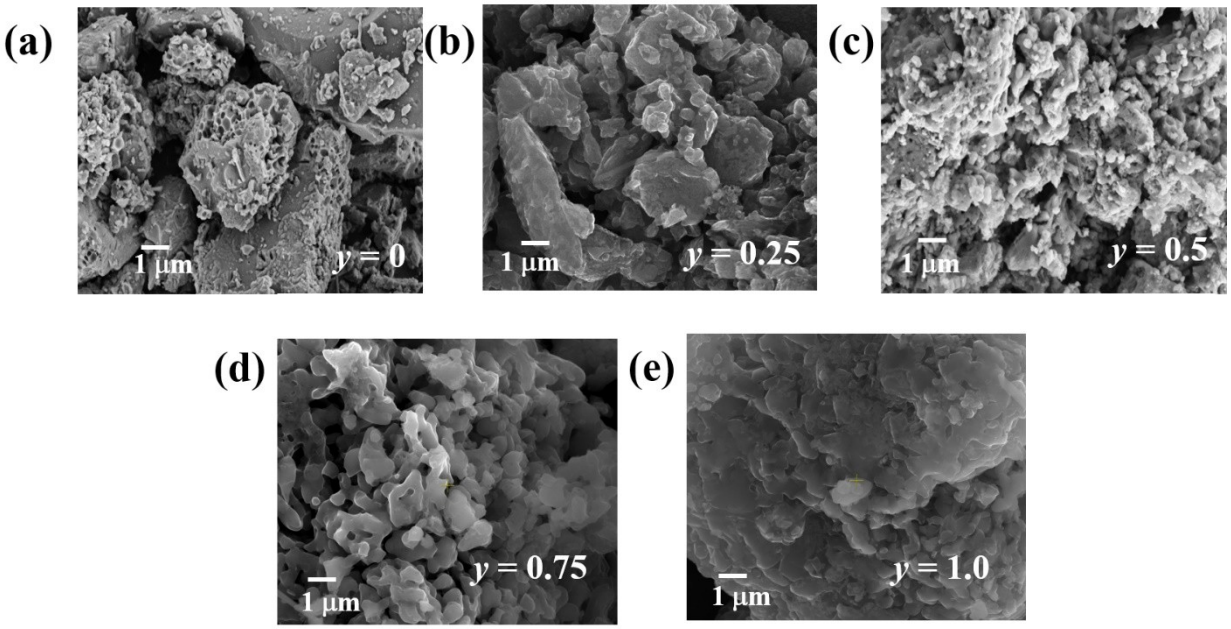

Figure S1. SEM images of NASICON-$Na_{3+y}V_{2-y}Mg_y(PO_4)_3$ cathodes.

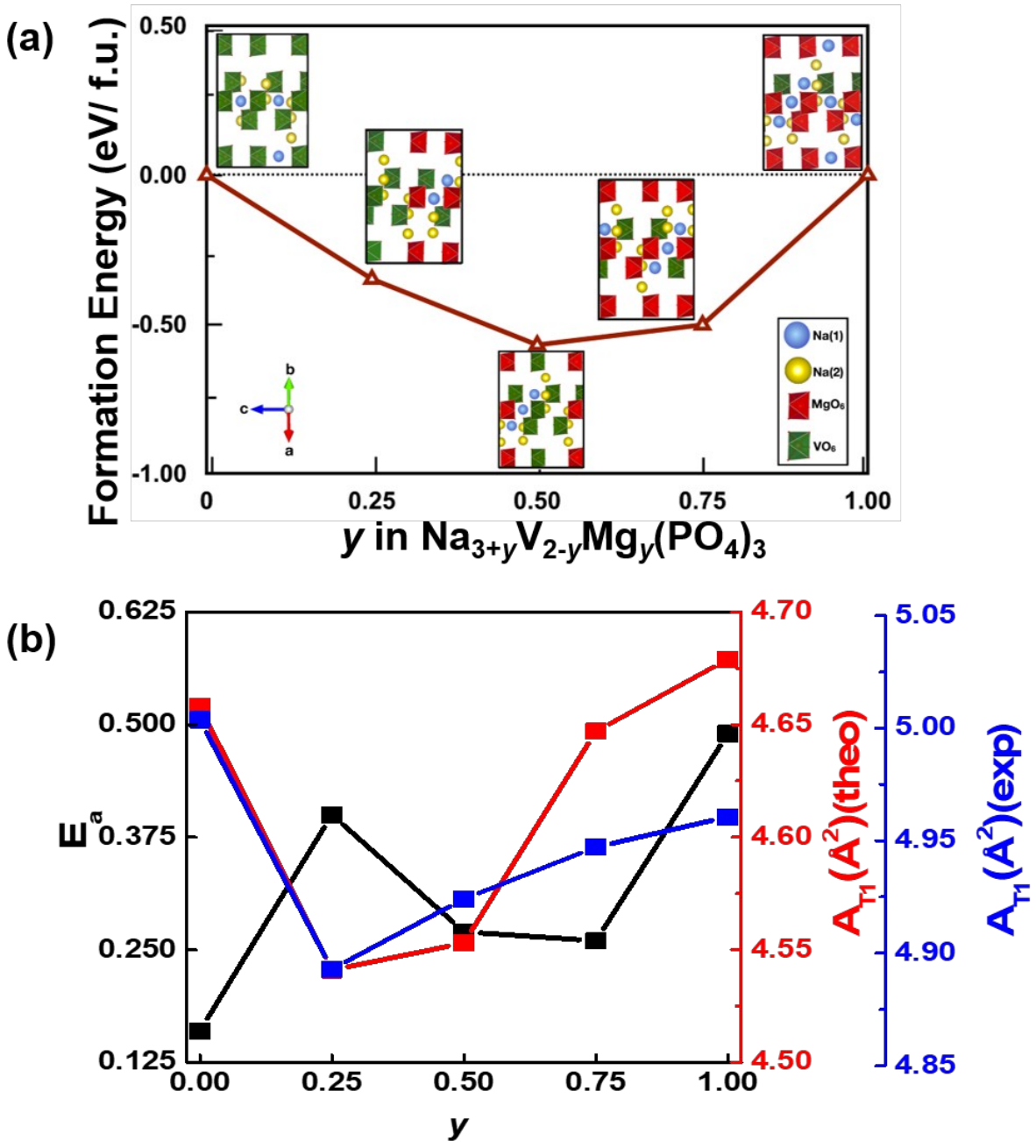

Figure S2. (a) Formation energies of the ground state $Na_{3+y}V_{2-y}Mg_y(PO_4)_3$ NASICON configurations as a function of *y*. The ground state structures are provided as insets. (b) Na^+ ion diffusion barriers (E_a) and diffusion bottleneck sizes (T1) computed for the ground state V/Mg and Na(1)/Na(2) orderings are plotted as a function of *y* in $Na_{3+y}V_{2-y}Mg_y(PO_4)_3$.

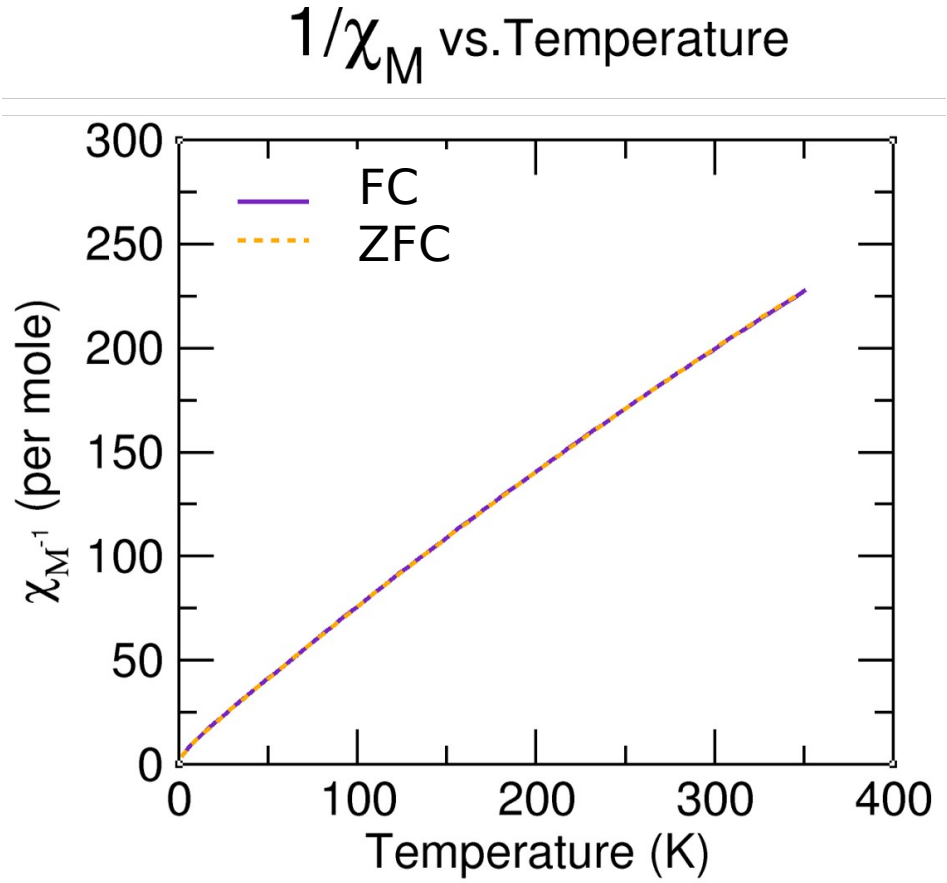

Figure S3. Experimental inverse magnetic susceptibility vs. temperature curve obtained from field cooled (FC) and zero field cooled (ZFC) magnetometry measurements on $y = 0$ cathode over the 2-350 K temperature range at a magnetic field strength of 1000 Oe.

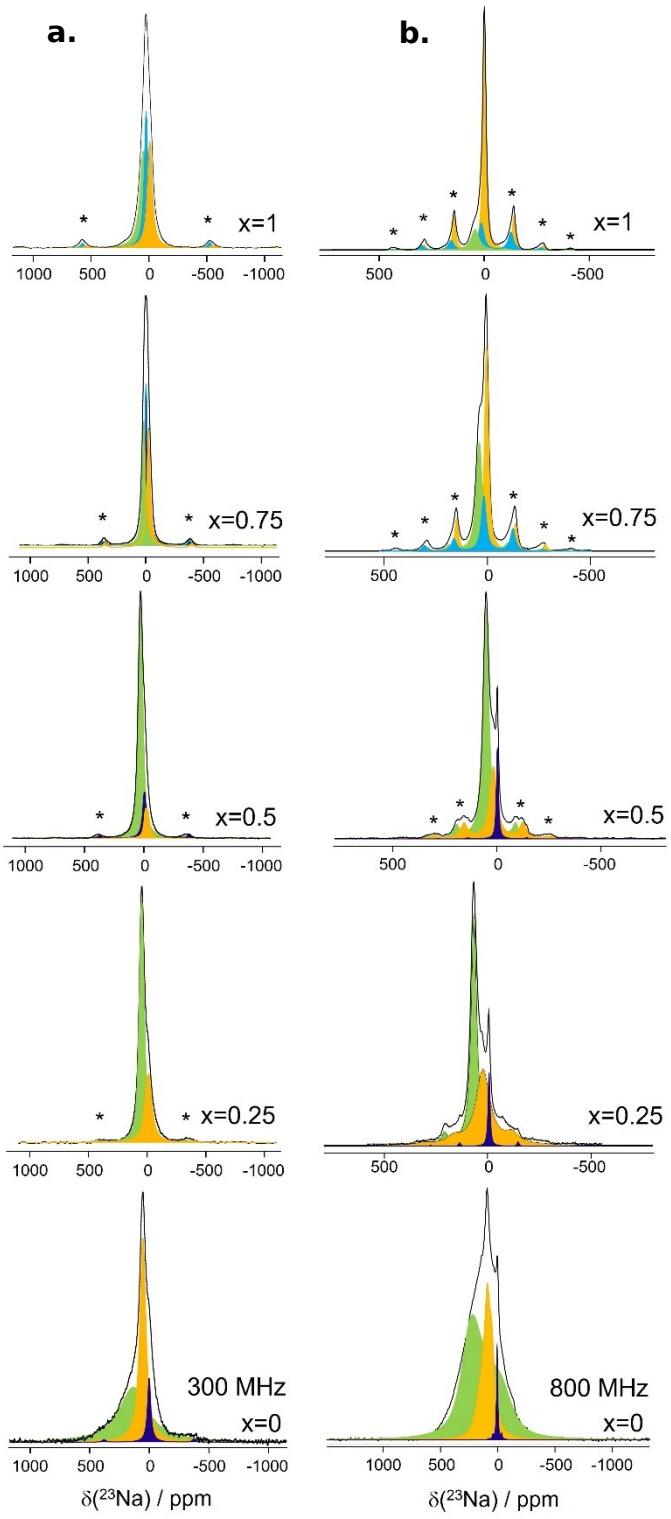

Figure S4. ^{23}Na NMR data collected on Mg-substituted $Na_{3+y}V_{2-y}Mg_y(PO_4)_3$ powder samples at **(a)** 7.05 T (300 MHz for ^{1}H) and **(b)** 18.8 T (800 MHz for ^{1}H). The yellow, green, light blue and dark blue signals in each spectrum correspond to the minimal set of ^{23}Na resonances that provide a satisfactory fit of the experimental data using a QUAD + CSA model. NMR parameters obtained from these fits are listed in Table S7. The dark blue signal at ca. 0 ppm in the data collected on y = 0, 0.25, and 0.5 samples is attributed to a diamagnetic impurity phase. This impurity phase is no longer clearly observed in spectra obtained on samples with

a higher Mg content. Resonances near 0 ppm in these spectra may instead be due to ^{23}Na nuclei predominantly surrounded by diamagnetic Mg^{2+} species in the paramagnetic NASICON phase, which is also be consistent with their greater linewidth compared to that of the dark blue signals in y = 0, 0.25 and 0.5 samples.

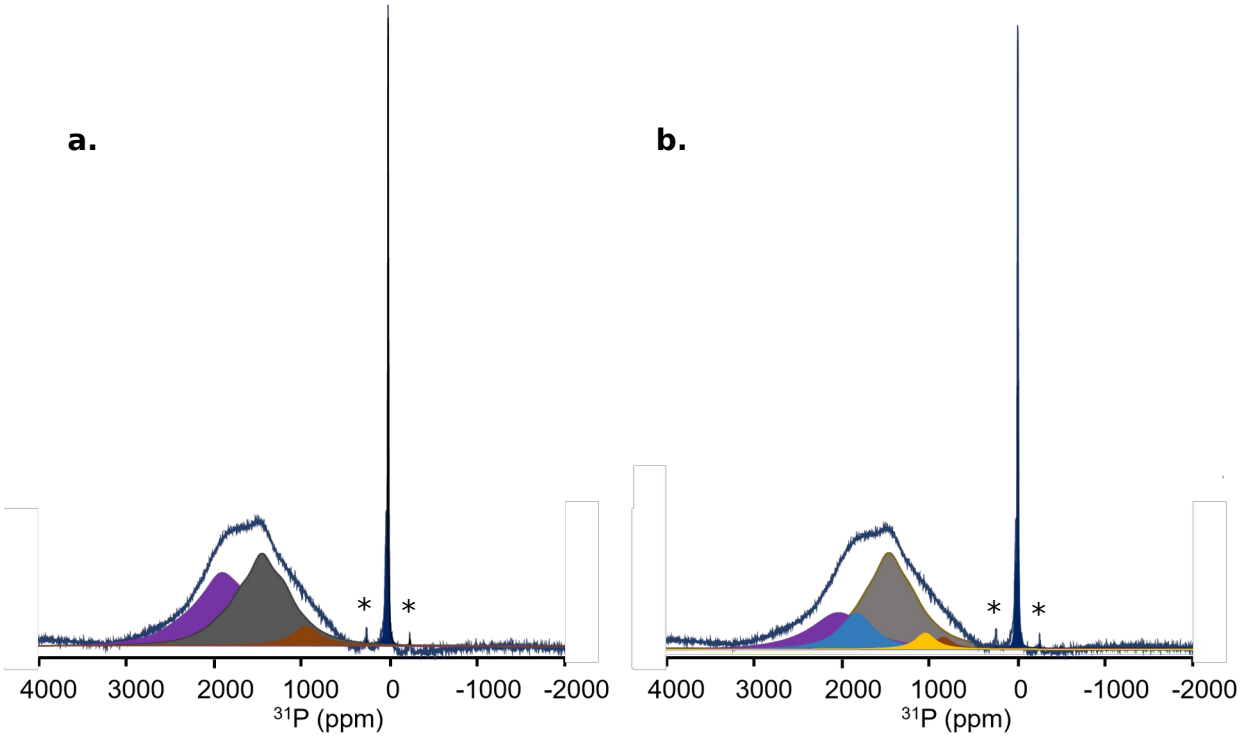

Figure S5. Example fits of the ^{31}P NMR data collected on the y = 0.5 pristine cathode: (a) using 3 environments and (b) using 5 environments. Both fits describe the observed lineshape equally well and highlight the ambiguity in fitting and assigning the spectra.

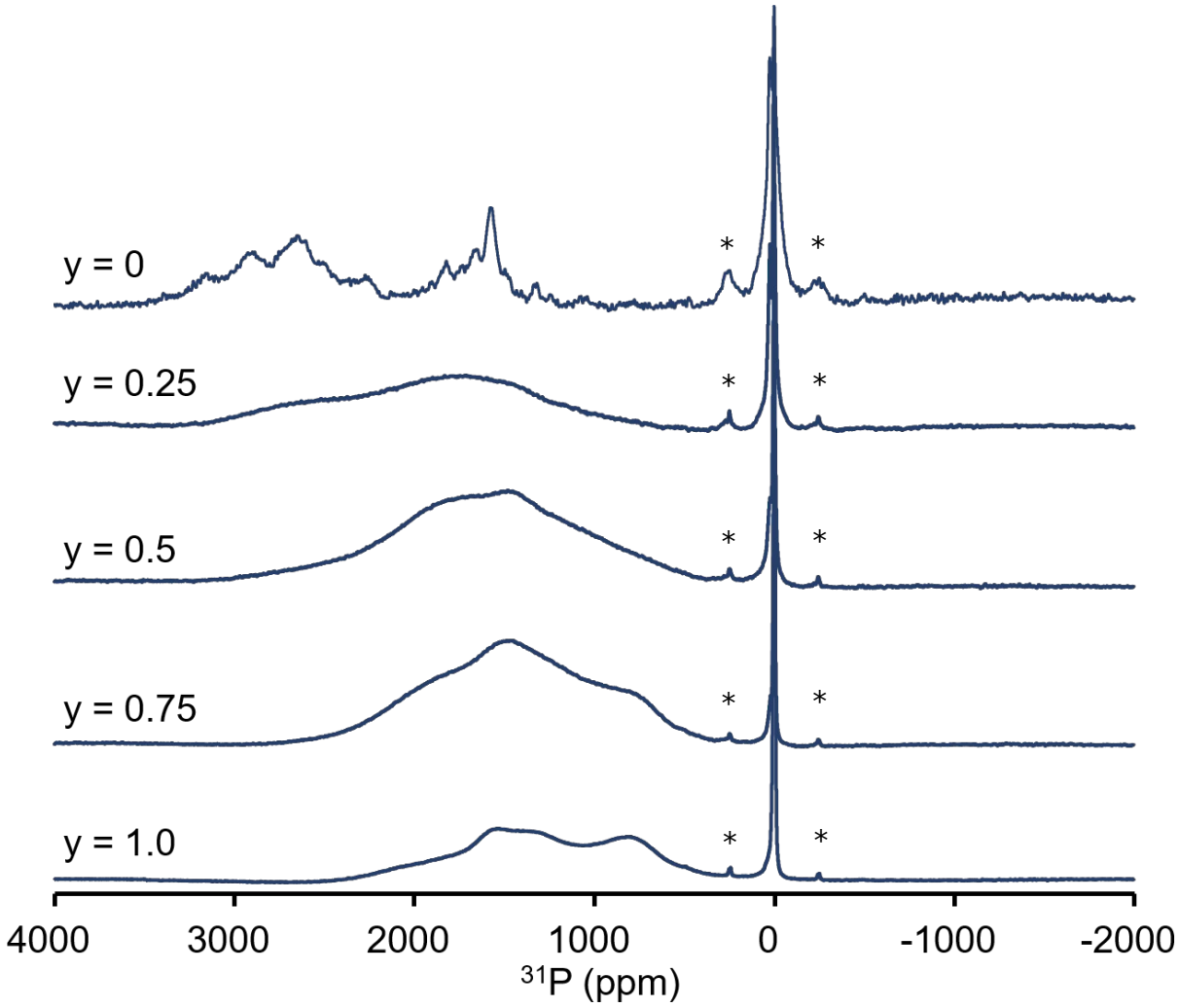

Figure S6. Full ^{31}P NMR spectra obtained on the series of pristine $Na_{3+y}V_{2-y}Mg_y(PO_4)_3$ cathode samples at 7.05 T and a spinning speed of 30 kHz. While resonances due to ^{31}P nuclei in the paramagnetic NASICON cathode appear above ~200 ppm, signals near 0 ppm (along with one spinning sideband on either side denoted with an asterisk) correspond to diamagnetic impurities, likely including Na_2HPO_4.

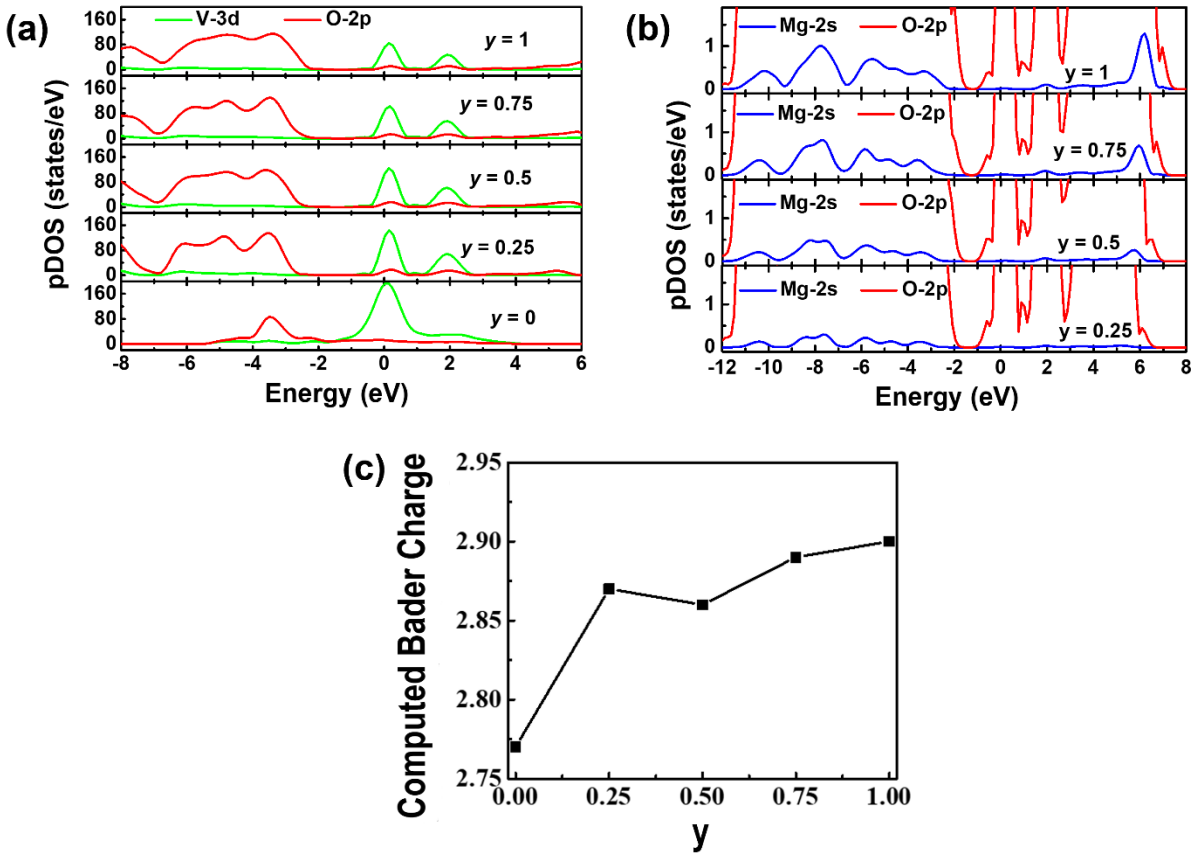

Figure S7. Calculated (a) and (b) pDOS and (c) Bader charges on vanadium in the $Na_{3+y}V_{2-y}Mg_y(PO_4)_3$ cathodes as a function of y.

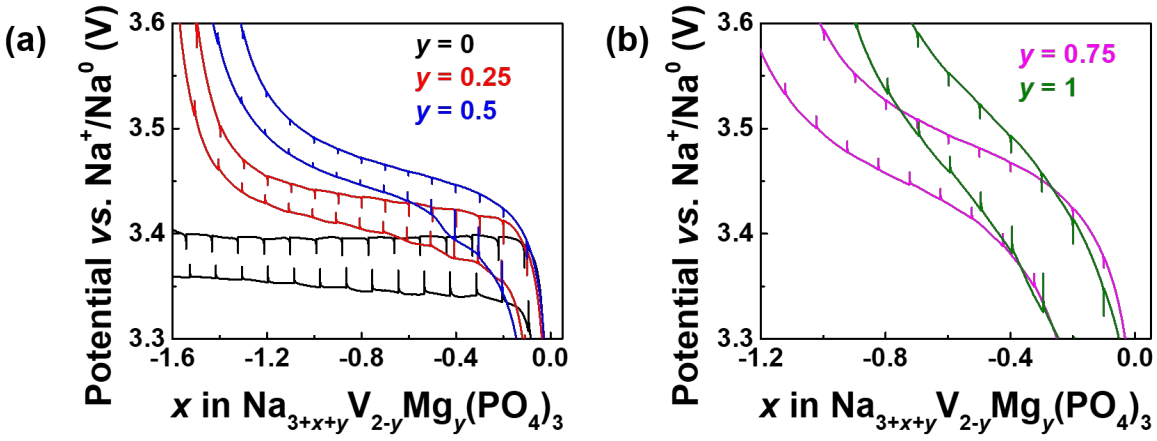

Figure S8. Enlarged views of the GITT profiles $Na_{3+y}V_{2-y}Mg_y(PO_4)_3$ cathodes.

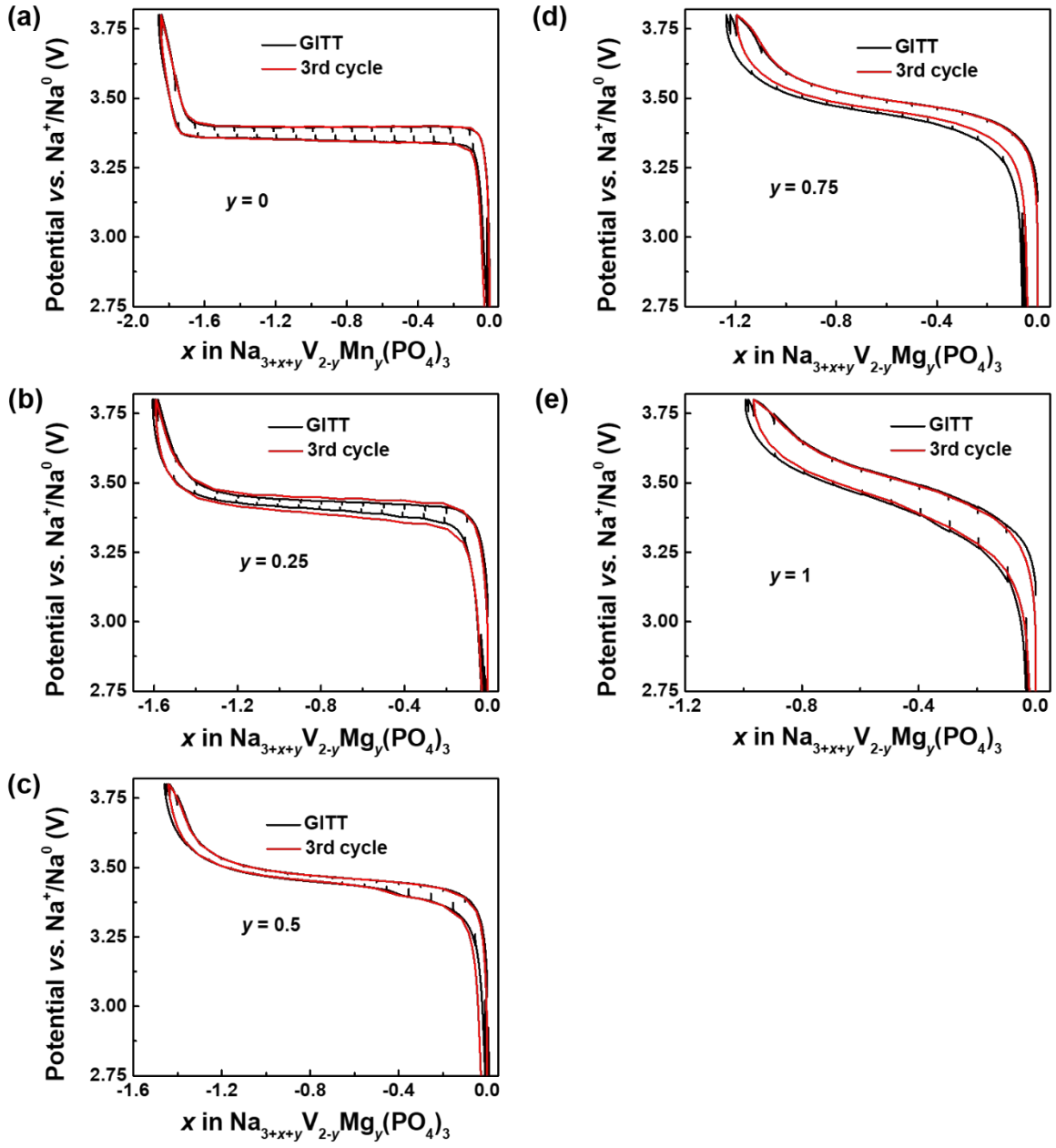

Figure S9. Comparison of voltage vs. composition profiles of $Na_{3+y}V_{2-y}Mg_y(PO_4)_3$ cathodes obtained from galvanostatic cycling (C/10 rate) and GITT protocols.

Table S1. Number of structural configurations generated using Supercell code and symmetrically unique structures considered for DFT calculations.

$Na_{3+y}V_{2-y}Mg_y(PO_4)_3$	**No. Of configurations generated from Supercell code**	**No. of symmetrically unique structures considered for DFT calculations**
***y* = 1**	924	100
***y* = 0.75**	8910	800
***y* = 0.50**	23,760	1200
***y* = 0.25**	11,016	600
***y* = 0**	1244	400

Table S2. Unit cell parameters obtained by Chotard et al.[16] for the experimental α-$Na_3V_2(PO_4)_3$ structure, and for the structures optimized using the H20 and H35 functionals in this work.

Structure	***a* / Å**	***b* / Å**	***c* / Å**	**α / °**	**β / °**	**γ / °**
EXP	15.124	8.729	21.614	90.0	90.2	90.0
OPT H20	15.232	8.790	21.577	90.0	90.1	90.0
OPT H35	15.176	8.756	21.494	90.0	90.1	90.0

Table S3. CHN elemental analysis of $Na_{3+y}V_{2-y}Mg_y(PO_4)_3$ samples

$Na_{3+y}V_{2-y}Mg_y(PO_4)_3$	**Carbon content (%)**
***y* = 0**	3.25
***y* = 0.25**	4.97
***y* = 0.5**	4.51
***y* = 0.75**	5.13
***y* = 1**	4.07

Table S4. Lattice parameters and bond distances obtained from the Rietveld analysis of the powder XRD patterns of $Na_{3+y}V_{2-y}Mg_y(PO_4)_3$ samples.

	***y* = 0**	***y* = 0.25**	***y* = 0.5**	***y* = 0.75**	***y* = 1**
Lattice parameters (Å)	*a* = 8.724(1) *c* =21.806(6)	*a* = 8.759 (17) *c* = 21.775 (7)	*a* = 8.807 (33) *c* = 21.671 (12)	*a* = 8.846(17) *c* = 21.558 (7)	*a* = 8.877 (15) *c* = 21.424 (6)
Na(1) occupancy	0.790	0.722	0.757	0.913	1
Na(2) occupancy	0.713	0.767	0.848	0.899	0.964
V–O average bond length (Å)	2.054(1) × 6	2.038(2) × 6	2.042(5) × 6	2.045(3) × 6	2.046 (5) × 6
Na(1)–O average bond length (Å)	2.431(1)× 6	2.424(1)× 6	2.423(1)× 6	2.420(1)× 6	2.415(1)× 6
Na(2)–O average bond length (Å)	2.433(1)× 2 2.443(1)× 2 2.886(1)× 2 2.613(1)× 2	2.418(2)× 2 2.471(2)× 2 2.879(1)× 2 2.609(1)× 2	2.431(1)× 2 2.485(1)× 2 2.889(0)× 2 2.601(1)× 2	2.443(1)× 2 2.492(1)× 2 2.901(1)× 2 2.591(1)× 2	2.451(1)× 2 2.502(1)× 2 2.904(0)× 2 2.579(1)× 2
Reliability factors	R_{wp} = 3.9% Chi^2 = 3.47	R_{wp} = 3.62% Chi^2 = 3.54	R_{wp} = 2.98% Chi^2 = 2.75	R_{wp} = 3.43% Chi^2 = 2.71	R_{wp} = 3.70% Chi^2 = 2.62

Table S5. Lattice parameters and bond distances obtained from DFT calculations of $Na_{3+y}V_{2-y}Mg_y(PO_4)_3$ samples (on 1x1x2 supercells).

$Na_{3+y}V_{2-y}Mg_y(PO_4)_3$	**a (Å)**	**c (Å)**	**V-O (Å)**	**Na(1)-O (Å)**	**Na(2)-O (Å)**
***y* = 0**	8.865	42.96	2.00	2.405	2.53, 2.58, 2.90, 2.92
***y* = 0.25**	8.868	42.930	2.01	2.400	2.51, 2.58, 2.91, 2.93
***y* = 0.5**	8.872	42.888	2.04	2.39	2.45, 2.48, 2.55, 2.92
***y* = 0.75**	8.871	42.904	2.06	2.40	2.48, 2.50, 2.55, 2.91
***y* = 1**	8.883	42.784	2.07	2.38	2.45, 2.51, 2.93, 2.91

Table S6. EXAFS parameters obtained from the fitting of $Na_{3+y}V_{2-y}Mg_y(PO_4)_3$ samples.

$Na_{3+y}V_{2-y}Mg_y(PO_4)_3$	Co-ordination shell	Distances between atoms (r±Δr) (Å)	S_0^2	σ^2(Å^2)
***y* = 0**	**V-O×3**	1.992 +0.071	0.76	0.00904
	V-O×3	1.926+0.096		0.00860
	V-P×6	3.399-0.069		0.03806
	V-Na(1)×3	3.137+0.019		0.01339
	V-Na(2)×3	3.845-0.013		0.01905
***y* = 0.25**	**V-O×3**	2.003 -0.013	0.82	0.00764
	V-O×3	1.947+ 0.018		0.00468
	V-P×6	3.148+ 0.011		0.04588
	V-Na(1)×3	3.409+ 0.058		0.00511
	V-Na(2)×3	3.846+0.058		0.00979
***y* = 0.5**	**V-O×3**	2.000 +0.019	0.87	0.00088
	V-O×3	1.961+0.043		0.00272
	V-P×6	3.411+ 0.012		0.00091
	V-Na(1)×3	3.151+ 0.087		0.01054
	V-Na(2)×3	3.856-0.038		0.00409
***y* = 0.75**	**V-O×3**	2.003 -0.011	0.89	0.00168
	V-O×3	1.990+0.023		0.00184
	V-P×6	3.413+ 0.017		0.001191
	V-Na(1)×3	3.156+ 0.019		0.00072
	V-Na(2)×3	3.857+ 0.082		0.00478
***y* = 1**	**V-O×3**	2.024+ 0.069	0.83	0.00389
	V-O×3	2.009+0.0167		0.00618
	V-P×6	3.444+ 0.023		0.00050
	V-Na(1)×3	3.189+ 0.0919		0.00982
	V-Na(2)×3	3.891- 0.0355		0.0297

Table S7. Observed chemical shifts and relative integrated intensities of the various ^{23}Na resonances determined from fits of the NMR data collected on $Na_{3+y}V_{2-y}Mg_y(PO_4)_3$ (y = 0, 0.25, 0.5, 0.75, 1.0) powder samples at (a) 7.05 T and (b) 18.8 T using a QUAD + CSA model.

(a)

7.05 T	**δ_{obs} (1) (ppm)**	**δ_{obs} (2) (ppm)**	**δ_{obs} (3) (ppm)**	**Rel. Integrated Ratios (S1 : S2 :S3)**
***y* = 0**	134	55	0	6.8 : 5.6 : 1.0
***y* = 0.25**	44	-14	0	34.7 : 11.7 : 1.0
***y* = 0.5**	26	-8	0	7.8 : 1.4 : 1.0
***y* = 0.75**	23	4	-17	1.0 : 1.3 : 1.1
***y* = 1**	10	-9	-30	1.2 : 1.1 : 1.0

(b)

18.8 T	**δ_{obs} (1) (ppm)**	**δ_{obs} (2) (ppm)**	**δ_{obs} (3) (ppm)**	**Rel. Integrated Ratios (S1 : S2 :S3)**
***y* = 0**	182	86	-1	Significant signal overlap prevents accurate estimation of relative integrated intensities
***y* = 0.25**	71	24	-3	9.3 : 9.0 : 1.0
***y* = 0.5**	51	20	-3	8.1 : 4.3 : 1.0
***y* = 0.75**	43	19	7	1.5 : 1.0 : 2.1
***y* = 1.0**	48	17	4	1.0 : 1.8 : 5.1

Significant differences are observed between the chemical shifts and relative intensities of the ^{23}Na resonances at 7.05 and 18.8 T. These discrepancies could be due to:

- differential motional averaging of the ^{23}Na NMR signals arising from Na(1)- and Na(2)-type local environments at 7.05 and 18.8 T. Indeed, signal averaging results from chemical exchange between various Na sites in the NASICON structure at a higher rate than the frequency separation between NMR resonances ($\Delta\nu$, in Hz) corresponding to the sites in exchange. $\Delta\nu$ (in Hz) scales with the magnetic field strength and signals that may be averaged out at 7.05 T could appear as distinct peaks at 18.8 T. That is, the NMR timescale is 2.67x faster at 18.8 T compared to 7.05 T;
- the second-order quadrupolar shift, introducing a field-dependence to the observed chemical shift ($\delta_{obs} = \delta_{iso} + \delta_Q$) of Na nuclei in Na(1) and Na(2) sites in the NASICON structure. This field-dependence in turn impacts the propensity for resonances corresponding to various Na environments in the samples to average out at 7.05 T vs. 18.8 T;
- differences in NMR signal relaxation times at 7.05 T and at 18.8 T, which has an effect on the relative intensities of the observed resonances.
- the difficulty of fitting overlapping NMR signals, and errors associated with these fits.

Table S8. First principles ^{23}Na NMR parameters computed for α-$Na_3V_2(PO_4)_3$ using the CRYSTAL17 code. NMR shifts are computed using two hybrid correlation-exchange functionals (H20 and H35), as it has been found that shifts computed using the H20 (H35) functional provide an upper (lower) bound to the experimentally-observed chemical shift.[13] The computed NMR properties have been scaled using a magnetic scaling factor $\Phi = 0.030755$, and are comparable to room temperature ^{23}Na NMR data obtained at an 7.05 T external magnetic field. There are five Na local environments in α-NVP, denoted Na(1a), Na(1b), Na(1c), Na(2a), and Na(2b), with multiplicities specified in parenthesis in the table below. δ_{iso} is the isotropic Fermi contact shift, $\Delta\delta$ and η are the electron-nuclear dipolar anisotropy and asymmetry parameters, respectively, C_Q is the quadrupolar coupling constant, η_Q is the quadrupolar asymmetry, δ_Q is the second-order quadrupolar shift, and $\delta_{obs} = \delta_{iso} + \delta_Q$ is the observed chemical shift.

Environment	Parameter	OPT H20	OPT H35
Na(1a) (x4)	δ_{iso}/ppm	297	195
	$\Delta\delta$/ppm	1609	1607
	η	0.1	0.1
	C_Q/MHz	-3.50	-3.32
	η_Q	0.1	0.0
	δ_Q/ppm	-49	-44
	$\delta_{iso}+\delta_Q$/ppm	248	152
Na(1b) (x8)	δ_{iso}/ppm	422	306
	$\Delta\delta$/ppm	1444	1450
	η	0.0	0.0
	C_Q/MHz	-4.28	-4.15
	η_Q	0.1	0.1
	δ_Q/ppm	-73	-69
	$\delta_{iso}+\delta_Q$/ppm	349	237
Na(2a) (x8)	δ_{iso}/ppm	88	-7
	$\Delta\delta$/ppm	1202	1209
	η	0.7	0.7
	C_Q/MHz	-3.73	-3.64
	η_Q	0.2	0.2
	δ_Q/ppm	-56	-54
	$\delta_{iso}+\delta_Q$/ppm	32	-60
Na(2b) (x8)	δ_{iso}/ppm	78	-24
	$\Delta\delta$/ppm	1040	1061
	η	1.0	0.9
	C_Q/MHz	-3.10	-3.05
	η_Q	0.4	0.3
	δ_Q/ppm	-40	-38
	$\delta_{iso}+\delta_Q$/ppm	39	-62
Na(2c)	δ_{iso}/ppm	231	108

(x8)	$\Delta\delta$/ppm	1249	1251
	η	0.6	0.6
	C_Q/MHz	-4.20	-4.10
	η_Q	0.1	0.1
	δ_Q/ppm	-70	-67
	$\delta_{iso}+\delta_Q$/ppm	161	41

Table S9. Analysis of the computed ^{23}Na NMR parameters for the assignment of the average resonances observed experimentally at 7.05 T.

OPT HYB20	**ppm**	**Intensity**
If average over Na(1) sites	316	1
If average over Na(2) sites	77	2
If average over Na(1a), Na(1b), Na(2c) sites	254	5
If average over Na(2a), Na(2b) sites	35	4
OPT HYB35	ppm	Intensity
If average over Na(1) sites	209	1
If average over Na(2) sites	-27	2
If average over Na(1a), Na(1b), Na(2c) sites	142	5
If average over Na(2a), Na(2b) sites	-61	4

If we average over the resonances for Na(1a), Na(1b), Na(2c) sites, and over the Na(2a) and Na(2b) sites from Table S7, we can account for the experimentally observed resonances at 134 and 55 ppm in the low-field (7.05 T) NMR data with a relative integrated intensity ratio equal to 1.21. This value of the relative integrated intensity ratio is close to the 1.25 ratio obtained from the multiplicity of the Na sites in the unit cell.

Table S10. P-O-V bond pathway geometries for PA, PB, PC, PD and PE inα-NVP. These are given for the H20 optimized (OPT) structure obtained from CRYSTAL17 calculations.

Interaction	Geometry	PA	PB	PC	PD	PE
1st	**d(P – V) / Å**	3.394 Å,	3.358 Å,	3.423 Å,	3.364 Å,	3.317 Å,
	P – O – V / °	136.45°	139.87°	139.88°	141.74°	138.46°
2nd	**d(P – V) / Å**	3.360 Å,	3.358 Å,	3.438 Å,	3.464 Å,	3.435 Å,
	P – O – V / °	139.73°	139.75°	146.69°	159.85°	162.32°
3rd	**d(P – V) / Å**	3.410 Å,	3.462 Å,	3.424 Å,	3.403 Å,	3.445 Å,
	P – O – V / °	148.77°	152.25°	157.40°	143.91°	140.32°
4th	**d(P – V) / Å**	3.448 Å,	3.463 Å,	3.370 Å,	3.420 Å,	3.440 Å,
	P – O – V / °	155.64°	152.53°	148.11°	146.53°	148.90°

Table S11. Predicted chemical shift differences between ^{31}P NMR signals associated with crystallographically-distinct P sites in the α-NVP structure (PA, PB, PC, PD and PE), and computed using the H20 and H35 functionals as implemented in the CRYSTAL17 code. ^{31}P chemical shift differences, rather than absolute ^{31}P chemical shifts, are considered here since our previous work [14]has shown that the former is more reliable than the latter. Computed NMR shifts have been scaled using a magnetic scaling factor $\Phi = 0.030755$, and are comparable to room temperature ^{31}P NMR data obtained at a 7.05 Texternal magnetic field. The chemical shift of a ^{31}P nucleus in a PC-type environment in α-NVP is used as a reference for the calculations of chemical shift differences, as it has the lowest absolute chemical shift. For example, the chemical shift difference between ^{31}P nuclei in PA and PC environments is denoted $\Delta\delta_{iso,AC}$.

Parameter	H20	H35	Average
$\Delta\delta_{iso,EC}$/ppm	618	370	494
$\Delta\delta_{iso,AC}$/ppm	1068	919	994
$\Delta\delta_{iso,BC}$/ppm	1392	1350	1371
$\Delta\delta_{iso,DC}$/ppm	1701	1453	1577

Table S12. Refined cell parameters and unit cell volumes of *ex-situ* $Na_{3+y}V_{2-y}Mg_y(PO_4)_3$ (y = 0.5 and 1.0) cathodes

$Na_{3.5}V_{1.5}Mg_{0.5}(PO_4)_3$ (S.G.: R$\bar{3}$c)							
	a (Å)	**c (Å)**	**V (Å^3)**	**Na(1) occupancy**	**Na(2) occupancy**	**R_{wp}**	**Chi^2**
Pristine	8.807(11)	21.672(5)	1455.6(3)	0.758(7)	0.848(2)	2.6%	2.12
Charged 3.8 V	8.528(13)	21.634(4)	1362.5(4)	0.742(3)	0.688(12)	3.02%	1.88
	8.620(2)	21.389(6)	1376.4(6)	0.702(17)	0.824(7)	2.33%	
Discharged 2.75 V	8.777(6)	21.672(2)	1446.0(2)	0.751(14)	0.839(6)	3.17%	3.92

$Na_4VMg(PO_4)_3$ (S.G.: R$\bar{3}$c)							
	a (Å)	**c (Å)**	**V (Å^3)**	**Na(1) occupancy**	**Na(2) occupancy**	**R_{wp}**	**Chi^2**
Pristine	8.851(11)	21.487(3)	1457.9(3)	0.981(8)	0.977(3)	2.19%	2.95
Charged 3.8 V	8.739(10)	21.563(3)	1426.2(3)	0.867(14)	0.688(3)	2.79%	2.49
Discharged 2.75 V	8.852(5)	21.454(14)	1456.00(15)	0.967(9)	0.953(4)	3.61%	4.26

References

1. Dovesi, R.; Saunders, V. R.; Roetti, C.; Orlando, R.; Zicovich-Wilson, C. M. ; Pascale, F.; Civalleri, B.; Doll, K.; Harrison, N. M.; Bush, I. J.; D'Arco, P.; Llunell, M.; Causà, M.; Noël, Y.; Maschio, L.; Erba, A.; Rerat M.; Casassa S. CRYSTAL17 User's Manual (University of Torino, Torino, **2017**).

2. Dovesi, R.; Erba, A.; Orlando, R.; Zicovich-Wilson, C. M.; Civalleri, B.; Maschio, L.; Rérat, M.; Casassa, S.; Baima, J.; Salustro, S.; Kirtman, B. Quantum-mechanical condensed matter simulations with CRYSTAL. *WIREs Comput Mol Sci.* **2018**, *8*, e1360.

3. Becke, A. D. Density-functional thermochemistry. III. The role of exact exchange. *J. Chem. Phys.* **1993**, *98*, 5648–5652.

4. Lee, C.; Yang, W.; Parr, R. Development of the Colic-Salvetti correlation-energy formula into a functional of the electron density. *Phys. Rev., B Condens. Matter* **1988**, *37*, 785–789.

5. Vosko, S. H.; Wilk, L.; Nusair, M. Accurate spin-dependent electron liquid correlation energies for local spin density calculations: a critical analysis. *Can. J. Phys.* **1980**, *58*, 1200–1211.

6. Stephens, P. J.; Devlin, F. J.; Chabalowski, C. F.; Frisch, M. J. Ab Initio Calculation of Vibrational Absorption and Circular Dichroism Spectra Using Density Functional Force Fields. *J. Phys. Chem.* **1994**, *98*, 11623–11627.

7. Corà, F. Alfredsson, M.; Mallia, G.; Middlemiss, D. S.; Mackrodt, W. C.; Dovesi, R.; Orlando, R.; The Performance of Hybrid Density Functionals in Solid State Chemistry. *Principles and Applications of Density Functional Theory in Inorganic Chemistry II*, Structure *and Bonding* **2004**, *113*, 171–232.

8. Muscat, J.; Wander, A.; Harrison, N. M. On the prediction of band gaps from hybrid functional theory. *Chemical Physics Letters* **2001**, *342*, 397–401.

9. Feng X.; Harrison, N. Magnetic coupling constants from a hybrid density functional with 35% Hartree-Fock exchange. *Phys. Rev. B* **2004**, *70*, 092402.

10. Middlemiss, D. S.; Lawton, L. M.; Wilson, C. C. A solid-state hybrid density functional theory study of Prussian blue analogues and related chlorides at pressure. *J. Phys.: Condens. Matter* **2008**, *20*, 335231.

11. Moreira, I. de P. R.; Illas, F.; Martin, R. Effect of Fock exchange on the electronic structure and magnetic coupling in NiO. *Phys. Rev. B* **2002**, *65*, 155102.

12. Kim, J.; Middlemiss, D. S.; Chernova, N. A.; Zhu, B. Y. X.; Masquelier, C.; Grey, C. P. Linking Local Environments and Hyperfine Shifts: A Combined Experimental and Theoretical ^{31}P and ^{7}Li Solid-State NMR Study of Paramagnetic Fe(III) Phosphates. *J. Am. Chem. Soc.* **2010**, *132*, 16825–16840.

13. Middlemiss, D. S.; Ilott, A. J.; Clément, R. J.; Strobridge, F. C.; Grey, C. P. Density Functional Theory-Based Bond Pathway Decompositions of Hyperfine Shifts: Equipping Solid-State NMR to Characterize Atomic Environments in Paramagnetic Materials. *Chem. Mater.* **2013**, *25*, 1723–1734.

14. Clément, R. J.; Pell, A. J.; Middlemiss, D. S.; Strobridge, F. C.; Miller, J. K.; Whittingham, M. S.; Emsley, L.; Grey, C. P.; Pintacuda, G. Spin-Transfer Pathways in Paramagnetic Lithium Transition-Metal Phosphates from Combined Broadband Isotropic Solid-State MAS NMR Spectroscopy and DFT Calculations. *J. Am. Chem. Soc.* **2012**, *134*, 17178–17185.

15. Schäfer, A.; Horn, H.; Ahlrichs, R. Fully optimized contracted Gaussian basis sets for atoms Li to Kr. *J. Chem. Phys.* **1992**, *97*, 2571.

16. Chotard, J.-N.; Rousse, G.; David, R.; Mentré, O.; Courty, M.; Masquelier, C. Discovery of a Sodium-Ordered Form of $Na_3V_2(PO_4)_3$ below Ambient Temperature. *Chem. Mater.* **2015**, *27*, 5982–5987.

17. Monkhorst H. J.; Pack, J. D. Special points for Brillonin-zone integrations. *Phys. Rev. B* **1976**, *13*, 5188-5192.

18. Carlier, D.; Ménétrier, M.; Grey, C.; Delmas, C.; Ceder, G. Understanding the NMR shifts in paramagnetic transition metal oxides using density functional theory calculations. *Phys. Rev. B* **2003**, *67*, 174103.